

# Topological phonon transport in an optomechanical system

Hengjiang Ren,<sup>1,2,3,\*</sup> Tirth Shah,<sup>4,5,\*</sup> Hannes Pfeifer,<sup>4,†</sup> Christian Brendel,<sup>4</sup> Vittorio Peano,<sup>4</sup> Florian Marquardt,<sup>4,5</sup> and Oskar Painter<sup>1,2,3,6</sup>

<sup>1</sup>*Thomas J. Watson, Sr., Laboratory of Applied Physics,  
California Institute of Technology, Pasadena, California 91125, USA*

<sup>2</sup>*Kavli Nanoscience Institute, California Institute of Technology, Pasadena, California 91125, USA*

<sup>3</sup>*Institute for Quantum Information and Matter,  
California Institute of Technology, Pasadena, California 91125, USA*

<sup>4</sup>*Max Planck Institute for the Science of Light, Staudtstrasse 2, 91058 Erlangen, Germany*

<sup>5</sup>*Department of Physics, Friedrich-Alexander Universität Erlangen-Nürnberg, Staudtstrasse 7, 91058 Erlangen, Germany*

<sup>6</sup>*AWS Center for Quantum Computing, Pasadena, California 91125, USA.<sup>‡</sup>*

(Dated: September 15, 2020)

Recent advances in cavity-optomechanics [1] have now made it possible to use light not just as a passive measuring device of mechanical motion [2], but also to manipulate the motion of mechanical objects down to the level of individual quanta of vibrations (phonons). At the same time, microfabrication techniques have enabled small-scale optomechanical circuits capable of on-chip manipulation of mechanical and optical signals [3–12]. Building on these developments, theoretical proposals have shown that larger scale optomechanical arrays can be used to modify the propagation of phonons, realizing a form of topologically protected phonon transport [12–16]. Here, we report the observation of topological phonon transport within a multiscale optomechanical crystal structure consisting of an array of over 800 cavity-optomechanical elements. Using sensitive, spatially resolved optical read-out [17, 18] we detect thermal phonons in a 0.325 – 0.34 GHz band traveling along a topological edge channel, with substantial reduction in backscattering. This represents an important step from the pioneering macroscopic mechanical systems work [19–23] towards topological phononic systems at the nanoscale, where hypersonic frequency ( $\gtrsim$  GHz) acoustic wave circuits consisting of robust delay lines [24] and non-reciprocal elements [25–27] may be implemented. Owing to the broadband character of the topological channels, the control of the flow of heat-carrying phonons, albeit at cryogenic temperatures, may also be envisioned.

Topology deals with features invariant to smooth deformations. The band structure for waves in a periodic medium may display such topological features, and this can have immediate consequences for transport along

boundaries, e.g. producing protected edge states [28]. In recent years, these conceptual insights, first acquired for electrons, were quickly expanded to cover arbitrary waves [29]. This includes, in particular, mechanical vibrations [13, 19–23, 25, 26, 30, 31], with their potential for far-reaching applications in signal processing and other domains when implemented in compact chip-scale acoustic devices. A very promising approach to lower the footprint for excitation and read-out, and to boost the sensitivity to high-frequency vibrations, is to use radiation pressure forces in so-called optomechanical crystals (OMCs) [32–35]. OMCs are patterned structures that can be engineered to yield large radiation-pressure coupling between cavity photons and phonons.

Here, we demonstrate the optomechanical detection of topological phonon transport in a multiscale OMC fabricated into the surface of a silicon microchip. In contrast to standard single-scale devices, the multiscale OMC consists of a superlattice structure, superimposing two patterns with very different but commensurate lattice spacings. This multiscale approach adds an extra degree of flexibility, decoupling the engineering of photonic and phononic modes. In our design, at the larger scale is a phononic crystal. Embedded within each unit cell of the phononic crystal is a smaller scale photonic crystal, which hosts a high- $Q$  optical nanocavity for optical read-out of phonons. Local changes within the OMC lattice of the phononic crystal unit cell are used to create topologically distinct mechanical domains, the boundary of which host phononic helical edge states based on the Valley Hall effect [36, 37]. The optomechanical arrays in this work consist of over 800 phononic unit cells, each with a corresponding optical mode for single-site resolution of phonon transport.

Images of a fabricated multiscale OMC structure are shown in Figs. 1a,b. In our design, a triangular lattice of snowflake-shaped holes with lattice spacing  $a_m = 16.02 \mu\text{m}$  is superimposed onto another triangular lattice of cylindrical holes with a much smaller spacing  $a_o = 450 \text{ nm}$ . This hole pattern has been etched into the thin (220 nm thickness) silicon device layer of a silicon-on-insulator (SOI) microchip. After releasing the underlying buried oxide layer, this produces an array of connected

\* These authors contributed equally to this work.

† Current Address: Institut für Angewandte Physik, Universität Bonn, Wegelerstrae 8, 53115 Bonn, Germany

‡ opainter@caltech.edu

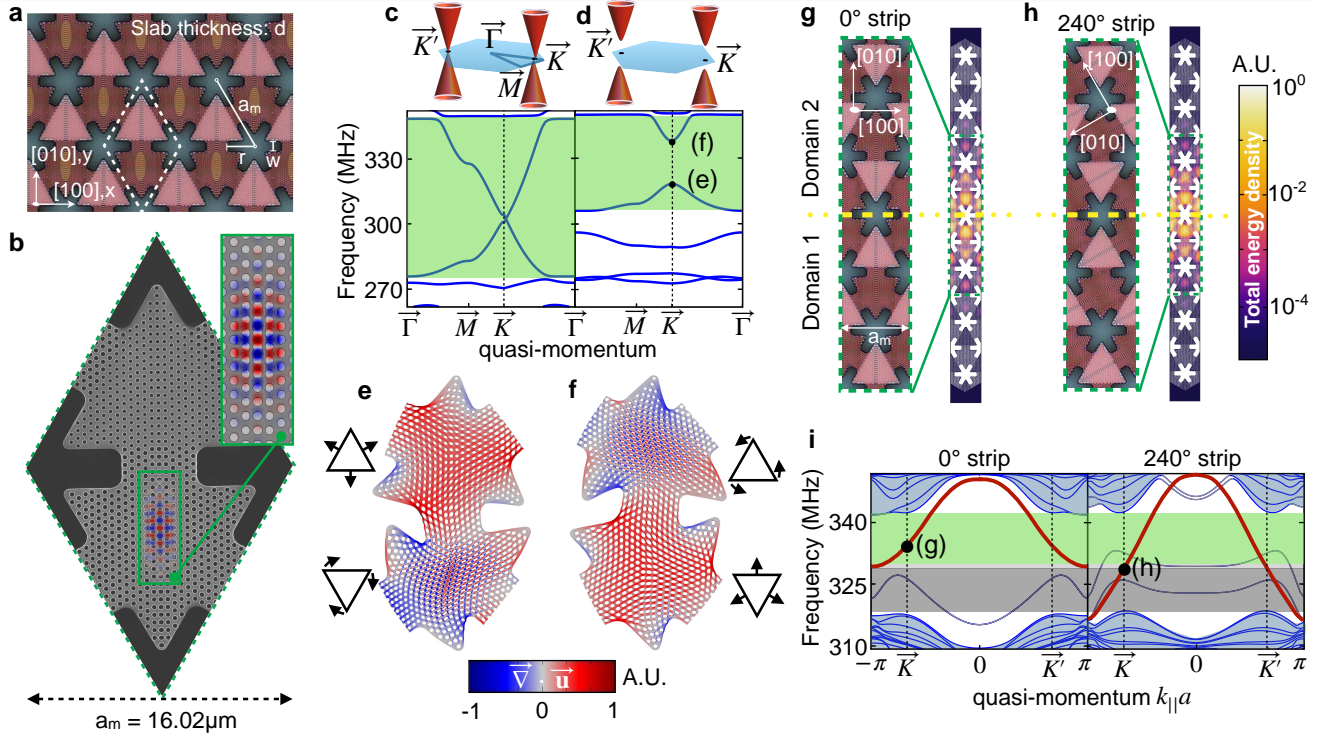


FIG. 1. **Design of the multiscale optomechanical crystal for topological phonics.** **a**, Optical microscope image showing the snowflake triangular lattice (unit cell dashed) with parameters  $(d, r, w, a_m) = (0.22, 5.77, 2.34, 16.02) \mu\text{m}$ . The axes are aligned with the silicon crystal. **b**, Focused Ion Beam (FIB) image of unit cell geometry with the simulated photonic-crystal cavity mode profile ( $E_{[100]}$  component of the electric field; red/blue indicates sign). **c** and **d**, Simulated phononic band structures with  $M_y$  mirror symmetry intact and broken (design in **b**), respectively. Inset: Sketches of the Dirac cones. **e**, **f**, Snapshots of the mechanical mode deformation (colours indicate the local volume change,  $\vec{\nabla} \cdot \vec{u}$ ; red corresponding to expansion and blue compression). The arrows in the associated pictograms indicate the dynamics of the motion. **g** and **h**, Optical microscope images and simulated mechanical mode profiles for two strip configurations, each comprising two topologically distinct domains (domain 1 as in **a**, **b**). The domain wall (dashed) has slope  $0^\circ$  (horizontal, **g**) or  $240^\circ$  (slanted, **h**) relative to the  $[100]$  axis. **i**, 1-D band structures calculated for the horizontal and slanted configurations. The red lines indicate the topological edge state dispersion, the grey lines are the additional edge state modes localized at the top and bottom boundaries of the geometry (away from the domain wall), the blue parts are bulk modes. The color shading inside the bulk band gap identifies different transport regimes in systems where the two types of domain walls are connected.

triangular silicon membranes forming the phononic crystal, each hosting a photonic crystal defined by the smaller holes (see Fig. 1b and inset). The snowflake pattern is adopted from a well-known single-scale OMC design [34, 35] and has also been proposed theoretically as a platform for topological phonics [14, 15]. In this work we have increased the snowflake lattice spacing by a factor of  $\sim 30$ , enabling every triangular membrane to harbor an optical nanocavity consisting of a localized defect in the triangular photonic crystal hole pattern. The purpose of using a cavity is to boost the optomechanical interaction (see App. E). In Fig. 1a and b, such a cavity is present only in the downward-pointing triangular membranes, with the upward-pointing triangular membranes having an unperturbed photonic crystal pattern. Although the two lattices (phononic and photonic) are at vastly different scales, the patterning of the photonic crystal within each triangular membrane does

(weakly) influence the phononic properties, providing an extra knob to trim the mechanical properties.

We employ these tuning knobs of the multiscale design to realize a structure supporting robust helical edge states based on the Valley Hall effect [36]. The Valley Hall effect is relevant for a wide range of systems that support Dirac cones, including electronic [36, 37], photonic [38], and mechanical systems [21, 22]. In this context, valley refers to the quasi-momentum region around a Dirac cone. In a time-reversal-symmetric system, the Dirac cones, and thus the corresponding valleys, come in pairs mapped onto each other by the operation of time reversal. Thus, the valley can be viewed as a binary degree of freedom akin to the spin. In the Valley Hall effect, valley-polarized edge excitations propagate in opposite directions, analogous to spin-polarized edge states in the Spin Hall effect.

As we are pursuing an optomechanical approach to the

detection of mechanical edge excitations, we focus here on the vibrational modes that couple to light, the in-plane modes which are even under the mirror operator  $M_z$  ( $z \mapsto -z$ ). For these modes, the snowflake phononic crystal supports a pair of Dirac cones well-isolated from the remaining bands [14, 15]. In our experiment, the Dirac cones have a center frequency of approximately 0.3 GHz, with linear Dirac-like dispersion across a bandwidth of 70 MHz (see Fig. 1c). These cones are protected by a symmetry under  $M_y$  (see App. F). We open the bulk band gap that will host the helical edge states by breaking this symmetry. Decreasing the size of the photonic-crystal holes in the upward-pointing triangles by a factor of 0.78 produces a band gap of width 18 MHz (see Fig 1d). The underlying vibrational Bloch waves, calculated using finite-element method (FEM) simulations (see App. C), are shown in Fig. 1e-f. A comparatively large unit-cell vacuum optomechanical coupling ( $g_0 = 2\pi \times 33.7\text{kHz}$ ) is produced for the higher-frequency mode in Fig. 1f because it displays breathing motion around the optical cavity. A detailed discussion of the optomechanical coupling is provided in App. E.

In the Valley Hall effect, the topological transport takes place through counter-propagating valley-polarized edge states which exist at the domain walls separating two topologically distinct domains of opposite so-called valley Chern number. By applying the mirror operation  $M_y$ , we construct from the deliberately mirror-symmetry-broken design described above, a second domain with opposite valley Chern numbers (see Fig. 1g,h). The key feature leading to robust transport is that edge excitations can navigate a path with arbitrarily sharp angles while still remaining confined within the same valley region of quasi-momentum space. On the other hand, backscattering would require large quasi-momentum transfer to reach a different valley, and is thus strongly suppressed. Our fit to the Dirac Hamiltonian describing our anisotropic structure (see App. A) shows both a dependence of the band structure on the domain wall orientation and some deviations from the idealized theoretical limiting case. For a horizontal domain wall, this leads to in-gap edge states that extend only through part of the full band gap (see Fig. 1i). Below we show that the transmission around sharp corners remains robust nevertheless, with this imperfection only reducing the relevant bandwidth.

We have fabricated several devices where an internal domain of type 2 is surrounded by an external domain of type 1. The ensuing closed domain wall produces a topological mechanical cavity. In a topological cavity, counter-propagating running waves remain decoupled in spite of sharp turns and/or disorder. This give rise to a characteristic spectrum formed by a series of doublets. These doublets are degenerate, with any slight lifting of the degeneracy due to residual inter-valley scattering.

The first topological cavity structure that we study is shown in Fig. 2a and Fig. 2b, consisting of an equilateral triangle of 28 snowflake unit cells along each side.

A schematic of our optical setup used to measure the phononic properties of the topological cavity structure is shown in Fig. 2c. A tunable external cavity diode laser coupled to an optical fiber taper is used to optically excite individual optical nanocavities within the multiscale OMC array. The out-coupled laser light, which contains the local mechanical motion of the structure imprinted as intensity modulations, is detected on a photodiode and analyzed on an electronic spectrum analyzer. Owing to the thermal nature of the measured mechanical motion in this work, the measured electronic spectrum analyzer signal represents a local mechanical noise power spectral density (NPSD). By moving the taper position we are able to address any unit cell of the larger-scale phononic lattice, obtaining a site-resolved spectrum of the thermally populated phonon modes (see App. B for further details). As an example, we show in the top plot of Fig. 2d the resulting optically-transduced local mechanical spectrum for an optical fiber taper position at site (d) in Fig. 2a, which is in the bulk region of domain 1. The measured spectrum is seen to be in close agreement with our theoretical predictions based on FEM simulations (bottom plot of Fig. 2d), both of which show a bulk band gap which covers an interval from 316 MHz to 338 MHz. We note that the amplitude of the thermal motion transduced in these measurements is only on order 10 fm, highlighting the sensitivity of our optical read-out scheme.

We now focus on the domain wall region. Exploiting our single-site resolution capability, we have measured the mechanical NPSD as a function of read-out position, as shown in Fig. 2e. This reveals two dramatically different transport regimes. For the mechanical cavity modes at lower frequencies (321 MHz - 327 MHz), we observe a strong modulation versus site position in each of the mechanical mode peaks. These fringe-like features indicate that thermal phonon excitations are reflected and form standing waves. This is due to the absence of topological edge modes inside the horizontal domain wall at these frequencies, resulting in standing waves inside the slanted domain wall portions of the mechanical cavity path. By contrast, we observe no such fringes in the higher-frequency regime (327 MHz - 337 MHz). This indicates backscattering-immune running waves, providing a direct visual signature of the formation of a topological mechanical cavity. Below, we refer to this frequency range as the topological bandwidth. In between these regimes, there is a crossover region (light grey in Figs. 2f-g), where the horizontal edge already supports edge states but backscattering is still possible because very small quasi-momentum transfers are sufficient to flip right-moving into left-moving horizontal edge states due to their proximity to the Brillouin zone boundary of the horizontal edge structure (see bandstructure plot in Fig. 1i).

We further substantiate the absence of backscattering in the topological bandwidth by comparing the frequency dependence of the measured NPSD with theory predic-

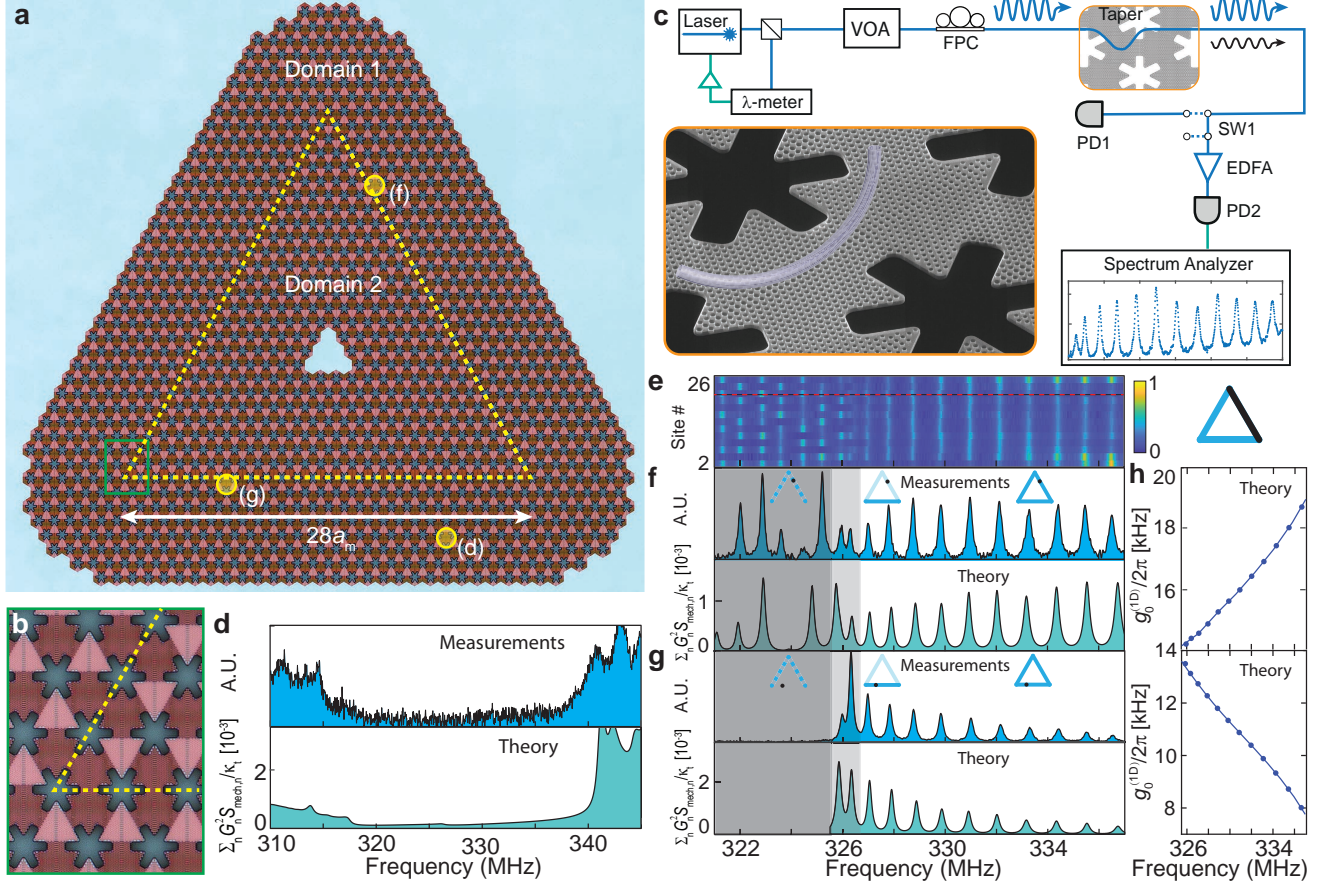


FIG. 2. **Characterization of topological edge states using optomechanical read-out.** **a**, Optical microscope image of triangular topological mechanical cavity (Domain wall: dashed line. Read-out cavities for the measurements in **d**, **f**, and **g**: yellow dots). **b**, Zoom-in of the topological cavity corner (green box in **a**). **c**, Experimental setup. Mechanical side-bands are imprinted on a laser beam transmitted through an optical cavity, detecting the NPSD of the mechanical waves. Acronyms: optical wave meter ( $\lambda$  meter), variable optical attenuator (VOA), fiber polarization controller (FPC), optical switch (SW), erbium-doped fiber amplifier (EDFA), photodetector (PD). **d**, **f**, and **g** Measured (top) and numerically estimated (bottom) NPSD, respectively, in the bulk of domain 1, on a slanted edge, and on a horizontal edge. Insets in **f**, and **g**: Sketches showing read-out positions and the expected local density of states. **e** Measured NPSD as a function of frequency and read-out position on a slanted edge (highlighted in black in the sketch). Red dashed line corresponds to the spectrum in **f**. The low-frequency region (dark grey in **f** and **g**) harbors modes only inside the slanted edges (cf. Fig. 1i). Data calibration is required to compare measurements from different read-out cavities (see App. J). **h**, Optomechanical coupling for edge states in slanted (top) and horizontal (bottom) domain walls (see App. I).

tions that assume perfect transmission at the corners. They are based on scattering matrix calculations that take FEM simulations as input (see App. I). The theoretical spectra are in good agreement with measurement results both on the slanted and the horizontal edges, as shown in Figs. 2f and 2g, respectively. Even the behaviour of the peak heights, distinctly different for both types of edges, is captured very well by including both the group velocity dispersion and the frequency-dependent vacuum optomechanical coupling  $g_0^{(1D)}$  (see Fig. 2h) in our analysis.

While the triangle geometry is the simplest closed-loop geometry, already producing a topological mechanical cavity, we also sought to test the robustness and immu-

nity to waveguide imperfections in more complex cavity structure where we could independently vary the length of waveguide segments in between sharp corners. The effects of such variations should be most pronounced in a geometry with appreciable backscattering at the corners, eventually producing separate standing wave patterns in the segments whose free spectral range would depend on the segment length. By contrast, the ideal case of robust topological transport should only be sensitive to the overall length of the domain wall circumference. Producing samples with different local geometrical details, but the same circumference, allows us to test these ideas by comparing their spectra.

To this end, we designed and fabricated two tree-

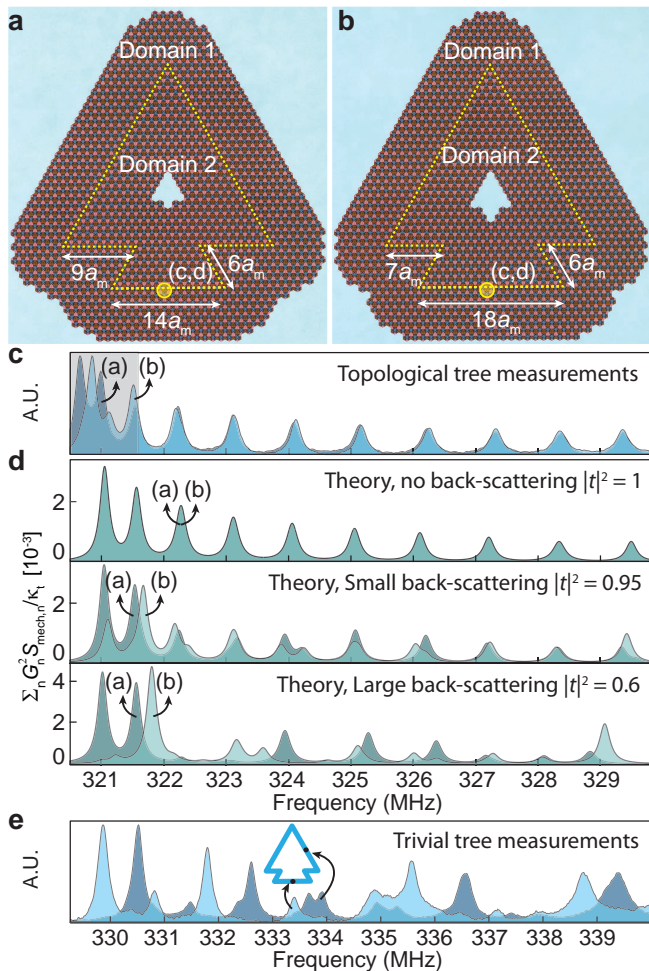


FIG. 3. **Robustness against backscattering.** **a** and **b**, Optical microscope image of two different tree-shaped topological mechanical cavities. **c**, Comparison of measurement results for the two tree-shaped topological cavities. **d**, Theoretical prediction for three backscattering strengths. Darker (lighter) spectra correspond to the tree-shaped topological cavities in **a** (**b**). In **c**, the cross-over region where backscattering can occur without requiring large quasi-momentum transfer is highlighted in light grey. **e**, Measurements for a trivial waveguide mechanical cavity (see App. L). Transduced NPSD measured at a slanted (dark blue) and a horizontal (light blue) edge, revealing strong backscattering.

shaped topological cavity structures. Each of these has a total domain wall circumference of  $96$  unit cells and includes seven  $60^\circ$  corners, but individual segment lengths differ. Figure. 3c shows the mechanical spectra measured near the horizontal edge of both tree geometries, superimposed onto each other. The most important observation is that, outside of the grey region, the two spectra agree almost perfectly, despite the different geometries.

This is a clear and direct experimental signature of the near-perfect absence of backscattering, as predicted for the topological edge states. The grey region is close to the band gap for the horizontal edge, where no suppression of backscattering is expected (see above).

In order to estimate the sensitivity of the spectra to backscattering, we performed calculations assuming varying levels of backscattering for both tree-shaped topological cavity geometries (Fig. 3d), where  $|t|^2$  ( $1 - |t|^2$ ) is the transmission (reflection) probability at each corner. These results show that even a small reflection probability of the order of 5% is enough to produce clearly visible differences between the spectra, including a splitting of the peaks. Both the direct measurements and the comparison with theory confirm that the phononic topological edge states robustly transmit through sharp corners.

For further comparison, we also designed and fabricated a tree-shaped trivial cavity. It is created by pulling a bulk band into the bulk band gap along a line defect embedded into an otherwise uniform domain 1 (see App. L for details). In this case, the mechanical spectra measured at two different locations (on a slanted and a horizontal edge) show signatures of backscattering from the sharp corners (see Fig. 3e), with irregular peak spacing and different peak locations for the two spectra.

In conclusion, we have demonstrated a multiscale optomechanical crystal and observed topological transport of thermal phonons in the  $0.3$  GHz band over a bandwidth of  $15$  MHz. This novel design opens the door to implementing on-chip phononic circuits [13, 15, 16, 39] with robust topological waveguides that have access to the full toolbox of optomechanics. Beyond cooling, mechanical lasing, sensitive read-out, and optical generation of nonclassical quantum states, this would also include the active optical control of topological circuits via local manipulation of mechanical modes (e.g., switching links between edge states). Another very promising avenue for applications consists in pushing towards even higher frequencies in the hypersonic regime up to  $100$  GHz should be possible with advanced lithographic methods inverting the scale hierarchy between photonics and phononics. This would allow one to manipulate thermal phonons in myriad of new ways, including broadband cooling of entire microscale objects, not just individual mechanical modes. Unidirectional edge channels like those found in a Chern insulator would allow one to implement thermal diodes, and, when supplemented by an energy pump, topologically protected phonon amplification and lasing [38, 40–42]. An exciting long-term perspective is to use topological phononic circuits as the basis of a new platform to explore quantum acoustodynamics for quantum information processing and storage, with coupling to dopants or superconducting qubits.

[1] M. Aspelmeyer, T. J. Kippenberg, and F. Marquardt, Rev. Mod. Phys. **86**, 1391 (2014).

[2] P. J. de Groot, Rep. Prog. Phys. **82**, 056101 (2019).

- [3] F. Massel, S. U. Cho, J.-M. Pirkkalainen, P. J. Hakonen, T. T. Heikkilä, and M. A. Sillanpää, *Nature communications* **3**, 1 (2012).
- [4] M. Zhang, S. Shah, J. Cardenas, and M. Lipson, *Phys. Rev. Lett.* **115**, 163902 (2015).
- [5] H. Xu, D. Mason, L. Jiang, and J. Harris, *Nature* **537**, 80 (2016).
- [6] P. Kharel, G. I. Harris, E. A. Kittlaus, W. H. Renninger, N. T. Otterstrom, J. G. E. Harris, and P. T. Rakich, *Science Advances* **5** (2019), 10.1126/sciadv.aav0582.
- [7] F. Ruesink, M.-A. Miri, A. Alu, and E. Verhagen, *Nature communications* **7**, 1 (2016).
- [8] G. A. Peterson, F. Lecocq, K. Cicak, R. W. Simmonds, J. Aumentado, and J. D. Teufel, *Physical Review X* **7**, 031001 (2017).
- [9] N. R. Bernier, L. D. Toth, A. Koottandavida, M. A. Ioannou, D. Malz, A. Nunnenkamp, A. Feofanov, and T. Kippenberg, *Nature communications* **8**, 604 (2017).
- [10] K. Fang, J. Luo, A. Metelmann, M. H. Matheny, F. Marquardt, A. A. Clerk, and O. Painter, *Nature Physics* **13**, 465 (2017).
- [11] H. Xu, L. Jiang, A. Clerk, and J. Harris, *Nature* **568**, 65 (2019).
- [12] J. P. Mathew, J. d. Pino, and E. Verhagen, *Nature Nanotechnology* **15**, 198 (2020).
- [13] V. Peano, C. Brendel, M. Schmidt, and F. Marquardt, *Physical Review X* **5**, 031011 (2015).
- [14] C. Brendel, V. Peano, O. J. Painter, and F. Marquardt, *Proceedings of the National Academy of Sciences* **114**, E3390 (2017).
- [15] C. Brendel, V. Peano, O. Painter, and F. Marquardt, *Physical Review B* **97**, 020102 (2018).
- [16] C. Sanavio, V. Peano, and A. Xuereb, *Phys. Rev. B* **101**, 085108 (2020).
- [17] J. D. Teufel, T. Donner, M. Castellanos-Beltran, J. W. Harlow, and K. W. Lehnert, *Nature nanotechnology* **4**, 820 (2009).
- [18] D. Wilson, V. Sudhir, N. Piro, R. Schilling, A. Ghadimi, and T. J. Kippenberg, *Nature* **524**, 325 (2015).
- [19] R. Süssstrunk and S. D. Huber, *Science* **349**, 47 (2015).
- [20] L. M. Nash, D. Kleckner, A. Read, V. Vitelli, A. M. Turner, and W. T. Irvine, *Proceedings of the National Academy of Sciences* **112**, 14495 (2015).
- [21] J. Lu, C. Qiu, L. Ye, X. Fan, M. Ke, F. Zhang, and Z. Liu, *Nature Physics* **13**, 369 (2017).
- [22] M. Miniaci, R. K. Pal, B. Morvan, and M. Ruzzene, *Phys. Rev. X* **8**, 031074 (2018).
- [23] S.-Y. Yu, C. He, Z. Wang, F.-K. Liu, X.-C. Sun, Z. Li, H.-Z. Lu, M.-H. Lu, X.-P. Liu, and Y.-F. Chen, *Nature Communications* **9**, 3072 (2018).
- [24] M. Hafezi, E. A. Demler, M. D. Lukin, and J. M. Taylor, *Nature Physics* **7**, 907 (2011).
- [25] J. Cha, K. W. Kim, and C. Daraio, *Nature* **564**, 229 (2018).
- [26] J. Ma, X. Xi, Y. Li, and X. Sun, arXiv preprint arXiv:2004.03067 (2020).
- [27] H. Nassar, B. Yousefzadeh, R. Fleury, M. Ruzzene, A. Alù, C. Daraio, A. N. Norris, G. Huang, and M. R. Haberman, *Nature Reviews Materials* , 1 (2020).
- [28] M. Z. Hasan and C. L. Kane, *Reviews of modern physics* **82**, 3045 (2010).
- [29] M. Aidelsburger, S. Nascimbene, and N. Goldman, *Comptes Rendus Physique* **19**, 394 (2018).
- [30] S. H. Mousavi, A. B. Khanikaev, and Z. Wang, *Nature Communications* **6**, 8682 (2015).
- [31] W. Deng, X. Huang, J. Lu, V. Peri, F. Li, S. D. Huber, and Z. Liu, *Nature communications* **11**, 1 (2020).
- [32] M. Eichenfield, J. Chan, R. M. Camacho, K. J. Vahala, and O. Painter, *Nature* **462**, 78 (2009).
- [33] A. H. Safavi-Naeini and O. Painter, *Opt. Express* **18**, 14926 (2010).
- [34] A. H. Safavi-Naeini, J. T. Hill, S. Meenehan, J. Chan, S. Gröblacher, and O. Painter, *Phys. Rev. Lett.* **112**, 153603 (2014).
- [35] H. Ren, M. H. Matheny, G. S. MacCabe, J. Luo, H. Pfeifer, M. Mirhosseini, and O. Painter, *Nature communications* **11**, 1 (2020).
- [36] I. Martin, Y. M. Blanter, and A. F. Morpurgo, *Phys. Rev. Lett.* **100**, 036804 (2008).
- [37] L. Ju, Z. Shi, N. Nair, Y. Lv, C. Jin, J. Velasco, C. Ojeda-Aristizabal, H. A. Bechtel, M. C. Martin, A. Zettl, J. Analytis, and F. Wang, *Nature* **520**, 650 (2015).
- [38] Y. Zeng, U. Chattopadhyay, B. Zhu, B. Qiang, J. Li, Y. Jin, L. Li, A. G. Davies, E. H. Linfield, B. Zhang, Y. Chong, and Q. J. Wang, *Nature* **578**, 246 (2020).
- [39] S. J. M. Habraken, K. Stannigel, M. D. Lukin, P. Zoller, and P. Rabl, *New J. Phys.* , 115004 (2012).
- [40] V. Peano, M. Houde, F. Marquardt, and A. A. Clerk, *Phys. Rev. X* **6**, 041026 (2016).
- [41] S. Mittal, E. A. Goldschmidt, and M. Hafezi, *Nature* **561**, 502 (2018).
- [42] M. A. Bandres, S. Wittek, G. Harari, M. Parto, J. Ren, M. Segev, D. N. Christodoulides, and M. Khajavikhan, *Science* **359**, eaar4005 (2018).
- [43] F. Zhang, A. H. MacDonald, and E. J. Mele, *Proceedings of the National Academy of Sciences* **110**, 10546 (2013).
- [44] F. Gao, H. Xue, Z. Yang, K. Lai, Y. Yu, X. Lin, Y. Chong, G. Shvets, and B. Zhang, *Nature Physics* **14**, 140 (2018).
- [45] J. R. Schaibley, H. Yu, G. Clark, P. Rivera, J. S. Ross, K. L. Seyler, W. Yao, and X. Xu, *Nature Reviews Materials* **1**, 16055 (2016).
- [46] J. K. Asbóth, L. Oroszlány, and A. Pályi, *A Short Course on Topological Insulators: Band Structure and Edge States in One and Two Dimensions*, Lecture Notes in Physics (Springer International Publishing, 2016).
- [47] COMSOL Multiphysics 5.3a, <http://www.comsol.com/>.
- [48] H. Sekoguchi, Y. Takahashi, T. Asano, and S. Noda, *Opt. Express* **22**, 916 (2014).
- [49] S. G. Johnson, P. R. Villeneuve, S. Fan, and J. D. Joannopoulos, *Physical Review B* **62**, 8212 (2000).
- [50] A. Chutinan and S. Noda, *Physical review B* **62**, 4488 (2000).
- [51] H. Huang, S. Zhou, and W. Duan, *Phys. Rev. B* **94**, 121117 (2016).
- [52] M. A. Hopcroft, W. D. Nix, and T. W. Kenny, *Journal of Microelectromechanical Systems* **19**, 229 (2010).
- [53] A. H. Safavi-Naeini and O. Painter, in *Cavity Optomechanics*, Quantum Science and Technology, edited by M. Aspelmeyer, T. J. Kippenberg, and F. Marquardt (Springer Berlin Heidelberg, 2014) pp. 195–231.

### Acknowledgements

The authors would like to thank Sameer Sonar and Utku Hatipoglu for the help with nanofabrication and measurement. This work was supported by the Gordon and Betty Moore Foundation (award #7435) and the Kavli

Nanoscience Institute at Caltech. H.R. was supported by the National Science Scholarship from A\*STAR, Singapore. T.S. and F.M. acknowledge support from the European Unions Horizon 2020 research and innovation programme under the Marie Skłodowska-Curie grant agreement No. 722923 (OMT). V.P. acknowledges support by the Julian Schwinger Foundation (Grant No. JSF-16-03-0000). F.M. acknowledges support from the European Unions Horizon 2020 Research and Innovation program under Grant No. 732894, Future and Emerging Technologies (FET)-Proactive Hybrid Optomechanical Technologies (HOT).

## Appendix A: Valley Hall Effect: Theoretical Model with Anisotropy

In the Valley Hall effect, the relevant topological invariant is the so-called valley Chern number  $C_v$  [36, 43]. The valley Chern number is defined within one valley in the framework of an effective two-band description and assumes two possible half-integer values,  $C_v = \pm 1/2$ . Interfaces between regions with opposite valley Chern numbers support in-gap valley-polarized edge states. Since the two valleys are mapped into each other by time-reversal, their edge states are counter-propagating.

We note that due to both our elongated cavity design and the anisotropic silicon crystal (see App. G), our system is not invariant under  $\mathcal{C}_3$ -rotations. This is a notable difference compared to previous larger-scale implementations of the valley Hall effect [21, 22, 37, 38, 44, 45]. Taking into account the residual bulk symmetry  $\mathcal{T}M_x$ , we find that our system is approximated by the effective two-band Dirac Hamiltonian (see App. F)

$$\hat{H}_D = \bar{\Omega} + (v_0 + v_x \hat{\sigma}_x) \hat{p}_x + v_y \hat{\sigma}_y \hat{p}_y + \{\Theta(\hat{\mathbf{r}}), (m + m' \hat{p}_x)\} \hat{\sigma}_z. \quad (\text{A1})$$

Here, we set  $\hbar = 1$ ,  $\hat{\sigma}_{x,y,z}$  are the Pauli matrices,  $\{\cdot, \cdot\}$  denotes the anti-commutator, and  $\Theta(\mathbf{r}) = 1/2$  ( $\Theta(\mathbf{r}) = -1/2$ ) inside domain 1 (domain 2). Moreover,  $\mathbf{p} = (p_x, p_y)$  is the quasi-momentum counted from a point on the  $k_x$ -axis where the Bloch waves are mapped into each other via  $M_y$ , see Fig. 1e,f. The most obvious difference to  $\mathcal{C}_3$ -symmetric systems is that the speed of the edge state now depends on the domain wall orientation. The solutions for slanted and horizontal domain walls and other surprising features are discussed in the App. F.

We now focus on the valley close to the  $\vec{K}$  point. Fixing the gauge by choosing  $\sigma_z = 1$  for the Bloch wave (f) (as shown in Fig. 1), a fit yields  $m = 2\pi \times 10.8\text{MHz}$ ,  $m'/a_m = -2\pi \times 5.4\text{MHz}$ ,  $v_x/a_m = 2\pi \times 12.5\text{MHz}$ , and  $v_y/a_m = 2\pi \times 14.9\text{MHz}$ . The valley Chern number for the lowest band is  $C_v = -\text{sign}(\Theta(\mathbf{r})mv_xv_y)/2$ , see App. F. Thus, we find  $C_v = -1/2$  ( $C_v = 1/2$ ) for domain 1 (domain 2). According to the bulk-boundary correspondence, the edge state will be a right-mover if one crosses the domain wall from domain 1 to domain 2 [46]. This is consistent with our strip FEM simulations, see Fig. 1i. The expansion leading to Eq. (A1) is valid if  $m/a_m \ll v_y, (v_x^2 + m'^2)^{1/2}$  (see App. F). This condition is not strictly fulfilled in our experiment, which leads to the deviations from the ideal case remarked upon in the Main Text.

## Appendix B: Measuring the mechanical thermal fluctuations

The thermal mechanical motion of phonons within the multiscale OMCs of this work are measured by driving the system with the laser locked to a blue detuning of 340 MHz from the optical nanocavity resonance. This frequency offset is chosen to align with the center frequency of the mechanical Dirac cones, increasing the sensitivity of the optical read-out for phonons propagating in the topological edge states. An optical fiber taper with a localized dimple region couples light evanescently into and out of an individual optical cavity with high efficiency. By moving the taper, we can address any unit cell of the larger-scale phononic lattice. Mechanical motion is imprinted on the phase of the laser light inside the optical nanocavity, which when extracted via the optical fiber taper maps the mechanical motion into intensity modulations in the transmitted laser light. The transmitted laser signal in the optical fiber is sent through an erbium-doped fiber amplifier (EDFA) to amplify the optical intensity modulations, and then onto a high-speed photoreceiver. The RF voltage from the photoreceiver is sent into a spectrum analyzer to determine the noise power spectral density (NPSD). The NPSD of the photocurrent contains a component proportional to the sum of the mechanical NPSD  $S_{\text{mech},n}$  of the mechanical normal modes of the structure, weighted by the square of the local optomechanical coupling  $G_n(\mathbf{j})$ , where  $n$  labels the mechanical mode and  $\mathbf{j}$  labels the (unit cell of the) read-out cavity (see App. H). Since only the vibrations within a single unit cell contribute to the optomechanical coupling  $G_n(\mathbf{j})$ , the transduced mechanical NPSD can be viewed as a (coarse-grained) mechanical local density of states.

## Appendix C: Finite Element Simulations

In Fig.1 of Main Text, we show the phononic band structures and the photonic crystal cavity modes. The mechanical normal modes are obtained by numerically solving the eigenvalue equation,

$$\text{div} \left[ \mathbf{C} : \left[ \text{grad } \mathbf{Q}_n(\mathbf{r}) + (\text{grad } \mathbf{Q}_n(\mathbf{r}))^T \right] \right] = -2\Omega_n^2 \rho(\mathbf{r}) \mathbf{Q}_n(\mathbf{r}). \quad (\text{C1})$$

Here and throughout the Appendix,  $\mathbf{Q}_n(\mathbf{r})$  ( $\mathbf{Q}_{\mathbf{k},n}(\mathbf{r})$ ) denotes the three-dimensional mechanical displacement  $\mathbf{Q}_n(\mathbf{r}, \mathbf{t}) = \text{Re} [\mathbf{Q}_n(\mathbf{r}) \cdot e^{-i\Omega_n \mathbf{t}}]$  for a normal mode (Bloch wave) with eigenfrequency  $\Omega_n$ . Moreover,  $\mathbf{C}$  is the elasticity tensor,  $\rho$  the mass density, and  $:$  is a symbol for the tensor product, where  $[\mathbf{C} : \text{grad } \boldsymbol{\psi}]_{ij} = C_{ijkl} \partial_l \psi_k$ .

Optically, our structure is described by the Maxwell's equations, which in the absence of a source, takes the form of the following eigenvalue equation

$$c^2 \text{curl} \left[ \frac{1}{\varepsilon(\mathbf{r})} \text{curl} \mathbf{H}_n(\mathbf{r}) \right] = \omega_n^2 \mathbf{H}_n(\mathbf{r}). \quad (\text{C2})$$

where  $\mathbf{H}_n(\mathbf{r})$  denotes the magnetic field  $\mathbf{H}_n(\mathbf{r}, \mathbf{t}) = \text{Re} [\mathbf{H}_n(\mathbf{r}) \cdot e^{-i\omega_n t}]$  for the photonic crystal cavity mode with eigenfrequency  $\omega_n$ .  $c$  is the speed of light in vacuum, and  $\varepsilon(\mathbf{r})$  is the relative permittivity of the medium. Both of these equations are solved with the finite-element method (FEM) solver [47].

#### Appendix D: Device fabrication

The devices were fabricated from a silicon-on-insulator (SOI) wafer (SEH, 220 nm silicon device layer, 3  $\mu\text{m}$  buried-oxide layer) using electron-beam lithography followed by inductively coupled plasma reactive ion etching (ICP/RIE). The devices were then cleaned by an oxygen plasma treatment before a final released in vapor-HF to remove buried-oxide layer. Note that the mechanical frequencies are different in the tree versus triangle cavity geometries, because parameters of the snowflake structures ( $a_m$ ,  $r$  and  $w$ ) in the tree geometries have been scaled by an overall factor of 1.02 with respect to the triangle cavity samples (the photonic crystal properties were kept identical).

#### Appendix E: Optical cavity design and characterization

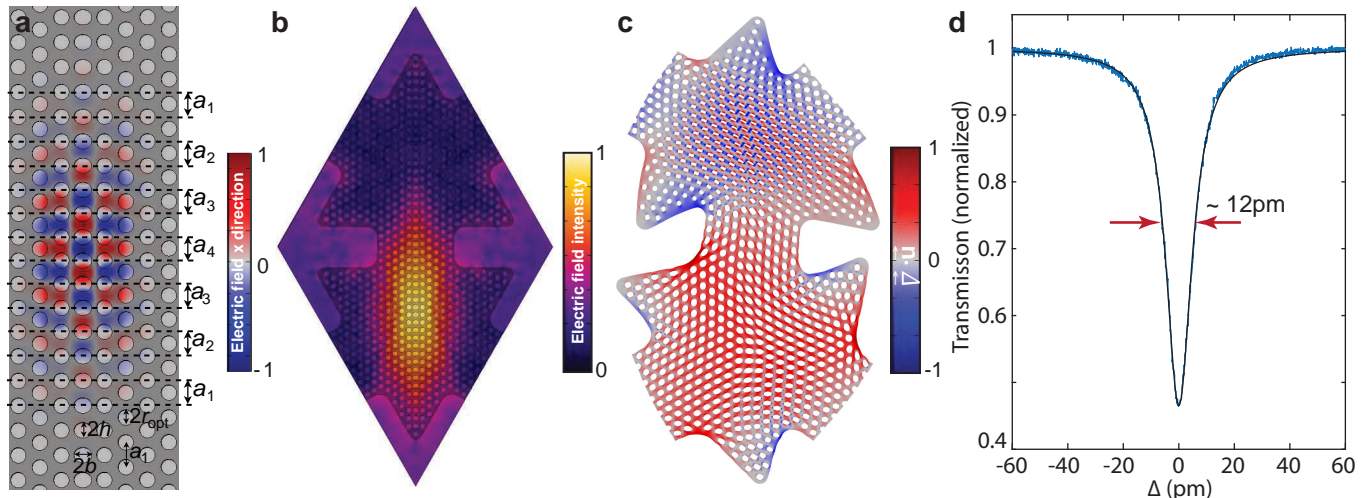


FIG. 4. **Optical cavity design and characterization.** **a**, Design of optical cavity, local lattice constant is increased smoothly from  $a_1 = 450\text{nm}$  to  $a_4 = 470\text{nm}$ . **b**, Optimum position of optical cavity in order to simultaneously achieve a large  $g_0$  and optical quality factor. **c**, Snapshots of the mechanical deformation at the degeneracy breaking point for upper band. The colours represent the change of volume ( $\vec{\nabla} \cdot \vec{u}$ ), with red (blue) corresponding to expansion (compression). **d**, Optical spectrum of a optical cavity measured using a swept laser scan.

The device in this work is designed around the silicon-on-insulator (SOI) materials platform, which naturally provides a thin Si device layer with typical widths of a few hundred nanometers. In our multiscale optomechanical crystal design, photonic crystal optical cavities are embedded inside the triangular membranes forming the larger scale snowflake phononic crystal. The role of the optical cavities is to amplify the radiation pressure force of the laser light. The radiation pressure force is given by  $\hbar G |a|^2$ , where  $G$  is the optomechanical frequency shift per displacement and  $|a|^2 = n_c$  is the number of intra-cavity photons.

Our optical cavity has been engineered starting from an existing design [48]. A cavity based on this design has displayed the highest observed optical quality factor reported in the literature ( $Q \sim 10^7$ ). Here, we have modified the original design to achieve a stronger coupling of the cavity resonance to the Dirac cone mechanical normal modes while maintaining the high optical quality factor. The underlying basic design is a triangular lattice of cylindrical holes.

An effective means of forming resonant cavities in such 2D slab photonic crystal structures is to weakly modulate the properties of a line-defect waveguide (W1 waveguide) [49, 50]. Leaky optical resonances are localized inside the slab and yet have wave vector components which radiate energy into the surrounding cladding, which is a major source of optical loss in real fabricated structures, causing light scattering out of the plane of the slab. A line-defect waveguide in a triangular lattice of cylindrical holes can be designed to have no leaky mode bands crossing the localized cavity mode frequency. In order to form a localized cavity resonance, the local lattice constant is increased smoothly from a nominal value of  $a_1 = 450$  nm to a value of  $a_4 = 470$  nm in the center of the cavity (see Fig. 4a), such that a localized resonance is created from shifting the higher frequency waveguide band into the bandgap.

The Dirac cone mechanical modes are in-plane modes with a breathing motion about the centre of the triangle. The change of volume ( $\nabla \cdot \vec{u}$ ) of such a mechanical breathing mode, simulated using FEM calculations, is shown in Fig. 4c. The mechanical breathing modes have naturally large optomechanical couplings, since breathing modes can efficiently interact with the optical cavity by moving the dielectric boundaries near the optical cavity as well as produce strain which overlaps with the electrical field of the optical resonance. In order to boost both the “moving-boundary” and the “photo-elastic” type of optomechanical coupling even further, we have added elliptical holes in the center of the W1 waveguide defect. Moreover, we have optimized the position of the center of the optical cavity along the  $y$ -axis in order to increase the optical quality factor ( $Q_{\text{opt}}$ ) within the limited triangular membrane region. This modification contributes as well to an increase of the optomechanical coupling.

The optical properties of the resonances of the optical cavities are determined by scanning the tunable laser across the  $\lambda = 1520 - 1570$  nm wavelength band, and measuring the transmitted optical power on a photodetector (PD1, cf. Main Text Fig. 2a). From the normalized transmission spectrum, the wavelength of the optical resonance, the total optical cavity decay rate, and the external coupling rate to the fiber taper waveguide for a device being tested can be determined. An example of the transmission spectrum is shown in Fig. 4d, where the optical cavity decay rate and external coupling rate are fitted to be  $\kappa/2\pi \approx 1.5$  GHz and  $\kappa_e/2\pi \approx 0.47$  GHz, respectively, corresponding to a loaded (extrinsic) optical  $Q_{\text{opt}}$  factor of  $\approx 129k$  ( $Q_{\text{opt,e}}$  of  $\approx 410k$ ).

Finally, the unit-cell single-photon optomechanical coupling strengths between the localized optical resonance and the two gapped Dirac cone modes in the unit cell geometry are calculated to be  $g_0/2\pi = 5.5$ kHz (lower band) and 33.7kHz (upper band).

## Appendix F: Theoretical description of the edge states using the Dirac equation

Here, we derive the Dirac Hamiltonian of the Main Text and solve for its eigenstates and eigenvalues.

### Derivation of the massless Dirac Hamiltonian

We first consider the special case in which Dirac cones are gapless. For our discussion only the in-plane symmetries are important. The general framework is a system with Wallpaper group cmm (point group  $\mathcal{C}_{2v}$ ) with a pair of Dirac cones on the  $k_x$ -axis. Since the two valleys are mapped one onto the other by the time-reversal symmetry it is entirely sufficient to discuss the dynamics for just one valley. Most of the discussion will be general but, when concreteness requires it, we focus on the valley whose degeneracy point lies on the positive  $k_x$ -axis in the first Brillouin zone (BZ).

For the cmm scenario, the point group includes the mirror symmetry  $M_y$  (with the mirror plane  $zx$ , flipping  $y \mapsto -y$ ). Since  $M_y$  does not change the quasi-momentum on the  $k_x$  axis, the Bloch waves can be chosen to be its eigenstates there. In other words, the bands on the  $k_x$ -axis can be labelled by their parity (odd or even) under  $M_y$ . Two bands with different parity are immune to level repulsion and they, thus, can cross leading to Dirac cones. The cones are robust because a perturbation that does not break  $M_y$  will slightly displace the crossing point but can not eliminate it. In the following we denote as  $\mathbf{Q}_+(\mathbf{r})$  (even) and  $\mathbf{Q}_-(\mathbf{r})$  (odd) the Bloch waves at the degeneracy point. By definition, we have

$$M_y \mathbf{Q}_\pm(\mathbf{r}) = \pm \mathbf{Q}_\pm(\mathbf{r}). \quad (\text{F1})$$

We note that  $M_y$  is the only unitary symmetry that maps one valley onto itself. The remaining unitary symmetries  $M_x$  and  $M_x M_y$  (a  $\pi$ -rotation about the  $z$ -axis) map the two partner valleys one onto the other and, thus, do not directly constrain the form of the Dirac Hamiltonian for a fixed valley. However, they do it indirectly when combined with the time-reversal symmetry  $\mathcal{T}$  to form the corresponding anti-unitary valley-preserving symmetries  $\mathcal{T} M_x$  and  $\mathcal{T} M_x M_y$ . In the following, we can choose to focus on  $\mathcal{T} M_x$  because a Hamiltonian that is invariant under  $M_y$  and  $\mathcal{T} M_x$  will automatically be invariant under  $\mathcal{T} M_x M_y$ . With the goal of constraining the form of the Dirac Hamiltonian as much as possible, we fix (at least partially) the complex phase of  $\mathbf{Q}_\pm(\mathbf{x})$  by requiring that

$$\mathcal{T} M_x \mathbf{Q}_\pm(\mathbf{x}) = \mathbf{Q}_\pm(\mathbf{x}). \quad (\text{F2})$$

We note that the above definition still allows to change the sign of  $\mathbf{Q}_+(\mathbf{x})$  and/or  $\mathbf{Q}_-(\mathbf{x})$ . In view of performing a two band approximation we define the basis,

$$\mathbf{Q}_{A/B,\mathbf{p}}(\mathbf{r}) = e^{i\mathbf{p}\cdot\mathbf{r}}\mathbf{Q}_{A/B}(\mathbf{r}), \quad \mathbf{Q}_{A/B}(\mathbf{r}) = \frac{1}{\sqrt{2}}(\mathbf{Q}_+(\mathbf{r}) \pm \mathbf{Q}_-(\mathbf{r})). \quad (\text{F3})$$

where  $\mathbf{p}$  is the quasi-momentum counted off from the degeneracy point. Note that by changing the sign of  $Q_+$  or  $Q_-$  (but not both signs at the same time) will swap the labels  $A$  and  $B$ . We mention in passing that the Bloch waves  $Q_{A,\mathbf{p}}$  and  $Q_{B,\mathbf{p}}$  transform under the cmm group symmetries in the same way as plane waves on each of the two sublattices of graphene. This should facilitate the reading to readers familiar with the Dirac equation in this more well known context.

In view of finding the form of the local Hamiltonian, one needs preliminarily to derive how the basis  $\mathbf{Q}_{A/B,\mathbf{p}}(\mathbf{r})$  transforms under the symmetry transformations  $M_y$  and  $\mathcal{T}M_x$ . From Eqs. (F1,F2,F3), we find

$$\begin{aligned} M_y \mathbf{Q}_{A,(p_x,p_y)}(\mathbf{r}) &= \mathbf{Q}_{B,(p_x,-p_y)}(\mathbf{r}), \\ \mathcal{T}M_x \mathbf{Q}_{A/B,(p_x,p_y)}(\mathbf{r}) &= \mathbf{Q}_{A/B,(p_x,-p_y)}(\mathbf{r}). \end{aligned} \quad (\text{F4})$$

Next, we introduce a set of Pauli matrices  $\hat{\sigma}_{i=x,y,z}$  such that  $\hat{\sigma}_z$  is diagonal on the  $A/B$  basis and  $\sigma_z = 1$  ( $\sigma_z = -1$ ) for  $\mathbf{Q}_{A,\mathbf{p}}(\mathbf{r})$  ( $\mathbf{Q}_{B,\mathbf{p}}(\mathbf{r})$ ). From Eqs. (F4) one, thus, see

$$M_y \hat{\sigma}_x M_y = \hat{\sigma}_x, \quad M_y \hat{\sigma}_{y/z} M_y = -\hat{\sigma}_{y/z}, \quad \mathcal{T}M_x \hat{\sigma}_{x/z} \mathcal{T}M_x = \hat{\sigma}_{x/z}, \quad \mathcal{T}M_x \hat{\sigma}_y \mathcal{T}M_x = -\hat{\sigma}_y. \quad (\text{F5})$$

while at the same time changing the quasi-momentum: under both  $M_y$  and  $\mathcal{T}M_x$  we have

$$(p_x, p_y) \rightarrow (p_x, -p_y). \quad (\text{F6})$$

Thus, for example the interaction  $p_x \hat{\sigma}_y$  will transform to  $-p_x \hat{\sigma}_y$  under the mirror symmetry  $M_y$  because  $\sigma_y$  changes sign, cf. F5, while  $p_x$  remains invariant, cf. Eqs. F6. Using Eqs. (F5) and (F6) we can easily determine the form of the Dirac equation. We are interested in a (small) region about the degeneracy point and, thus, we can restrict ourselves to linear terms in the quasi-momentum. Considering all possible linear terms and keeping only those that are invariant under both  $M_y$  and  $\mathcal{T}M_x$ , we arrive at the massless Dirac Hamiltonian

$$H_D = \bar{\Omega} + (v_0 + v_x \hat{\sigma}_x) p_x + v_y \hat{\sigma}_y p_y. \quad (\text{F7})$$

This gives rise to gapless cones described by the band structure

$$\Omega_{e/g} = \bar{\Omega} + v_0 p_x \pm \sqrt{(v_x p_x)^2 + (v_y p_y)^2}. \quad (\text{F8})$$

Compared to the standard setting with  $\mathcal{C}_3$  symmetry, here, the speed depends on the direction (because  $v_x \neq v_y$ ). Moreover, in the same direction the speed is different for the ground and excited band (because  $v_0 \neq 0$ ). Above the critical value of  $|v_0|$ ,  $|v_0| = |v_x|$ , the band structure become qualitatively different leading to so-called type II Dirac cones [51]. For type II cones there is a direction where the speed is zero for one of the two bands. In the following, we do not discuss further this scenario as our experiment is in the regime where  $|v_0| < |v_x|$ .

### Derivation of the full Dirac Hamiltonian within one domain

Next, we consider the case where the mirror symmetry  $M_y$  is broken but  $M_x$  is still a symmetry. Thus, the relevant Wallpaper group is now cm (point group  $\mathcal{C}_v$ ). Using Eqs. (F5) and (F6) to find all possible terms that preserves the symmetry  $\mathcal{T}M_x$ , we arrive at the Dirac Hamiltonian

$$H_D = \bar{\Omega} + (v_0 + v_x \hat{\sigma}_x) \hat{p}_x + v_y \hat{\sigma}_y \hat{p}_y + (m + m' \hat{p}_x) \sigma_z. \quad (\text{F9})$$

This give rise to the band structure

$$\Omega_{e/g} = \bar{\Omega} + v_0 p_x \pm \sqrt{(m + m' p_x)^2 + (v_x p_x)^2 + (v_y p_y)^2}. \quad (\text{F10})$$

We note that within the expansion in  $\mathbf{p}$  that underlies the Dirac Hamiltonian, we must assume  $|m' p_x| \ll |m|$ . Moreover, when the design with broken  $M_y$ -symmetry is obtained by modifying a design with conserved  $M_y$  symmetry (as in

our case) all the parameters in Eq. (F7) are renormalized, including the point on the  $k_x$ -axis from which the quasi-momentum is counted. We also note that for  $p_x = p_y = 0$  in Eq. (F9) the Bloch waves are eigenstates of  $\sigma_z$ . Since  $\sigma_z$  is by definition diagonal in the A/B basis from Eq. (F4) it follows that for this particular quasi-momentum the Bloch waves are mirror-symmetric partners of each other. This feature can serve as a definition of the origin  $p_x = 0$ . This implies that the Bloch waves shown in Fig. 1(e-f) of the Main Text, which look very much like mirror-symmetric partners in the  $xz$  plane, have displaced quasi-momentum  $\mathbf{p}$  very close to the origin. Once the point where  $p_x = 0$  is known, we use Eq. (F10) to fit the parameters in the Dirac Hamiltonian (the fitted values are given in the Main Text). We note that this way of fitting does not allow to fix the sign of  $v_x$ ,  $v_y$ , and  $m$ . In particular, the sign of  $mv_xv_y$  is still unknown. As we discuss below this sign fixes the value of the valley Chern number and to be able to determine it, it is not enough to examine the band structure alone but one rather needs to have information regarding the Bloch waves, see below.

### Berry curvature and Valley Chern numbers

It is convenient to introduce the set of rotated Pauli matrices

$$\tau_x = \frac{v_x}{\sqrt{v_x^2 + m'^2}}\sigma_x + \frac{m'}{\sqrt{v_x^2 + m'^2}}\sigma_z, \quad \tau_y = \sigma_y, \quad \tau_z = \frac{v_x}{\sqrt{v_x^2 + m'^2}}\sigma_z - \frac{m'}{\sqrt{v_x^2 + m'^2}}\sigma_x. \quad (\text{F11})$$

In terms of the new set of Pauli matrices, the Dirac Hamiltonian Eq. (F9) takes the simpler form

$$H_D = \bar{\Omega} + (v_0 + V_x \hat{\tau}_x)(\hat{p}_x - p_x^{(0)}) + V_y \hat{\tau}_y \hat{p}_y + M \tau_z, \quad (\text{F12})$$

$$V_x = (v_x^2 + m'^2)^{1/2}, \quad V_y = v_y, \quad M = \frac{mv_x}{V_x}, \quad p_x^{(0)} = -\frac{mm'}{V_x^2}. \quad (\text{F13})$$

The band structure in terms of the rescaled parameters reads

$$\Omega_{e/g} = \bar{\Omega} + v_0 p_x \pm \sqrt{M^2 + V_x^2 (p_x - p_x^{(0)})^2 + (V_y p_y)^2}. \quad (\text{F14})$$

Thus,  $p_x^{(0)}$  is the bottom of the valley where the band splitting is minimum (when counted off from the quasi-momentum where the two Bloch waves are one the mirror symmetry of the other in the  $zx$ -plane) and  $M$  is the bulk band gap.

The Berry curvature for the lowest band of the Dirac Hamiltonian is (see [46] for the first equality)

$$\mathcal{B}(\mathbf{p}) = -2\text{Im} \frac{\langle g, \mathbf{p} | \nabla_{p_x} H_D(\mathbf{p}) | e, \mathbf{p} \rangle \langle e, \mathbf{p} | \nabla_{p_y} H_D(\mathbf{p}) | g, \mathbf{p} \rangle}{(\Omega_e(\mathbf{p}) - \Omega_g(\mathbf{p}))^2} = \frac{MV_x V_y}{2 \left( M^2 + V_x^2 (p_x - p_x^{(0)})^2 + (V_y p_y)^2 \right)^{3/2}}, \quad (\text{F15})$$

where  $|g, \mathbf{p}\rangle$  and  $|e, \mathbf{p}\rangle$  are the ground and excited Bloch waves, respectively. As usual, the Chern number is defined as an integral of the Berry curvature [46]. For the valley Chern number, the integral over the BZ is replaced by an integral over the 2D plane,

$$C_v = -\frac{1}{2\pi} \int d^2 \mathbf{p} \mathcal{B}(\mathbf{p}) = -\frac{1}{2} \text{sgn}(mv_x v_y). \quad (\text{F16})$$

### Limits of validity of the Dirac approach

The valley Chern numbers are well defined if the Berry curvature of the real bands is strongly peaked in an isolated region surrounded by a small Berry curvature region. In fact, it makes sense to identify each valley exactly with such isolated large Berry curvature region. The Berry curvature as calculated using the Dirac Hamiltonian is peaked in an ellipse-shaped region with axes  $M/V_x$  and  $M/V_y$  about  $\mathbf{p} = (p_x^{(0)}, 0)$ , cf. Eq. (F15). We have to require that this region remains within the quasi-momentum region where the linear expansion leading to the Dirac equation is valid. The typical size of this region is  $\sim 1/a_m$ . We, thus, arrive to the condition,

$$M/a_m \ll V_x, V_y. \quad (\text{F17})$$

### Identifying the valley Chern numbers from FEM simulations

Next, we want to determine the valley Chern number for our particular structure. We aim to use the formula  $C_v = -\frac{1}{2}\text{sgn}(mv_xv_y)$  and use some limited input from our FEM simulations to identify the sign of  $mv_xv_y$ . As discussed above our definitions Eqs. (F1,F2,F3) have the disadvantage of not completely fixing the gauge in the Dirac equation: we have the freedom to identify either of the Bloch waves in Fig. 1(e,f) with  $\mathbf{Q}_A$ . Swapping the two states will have the effect of changing the sign of both  $m$  and  $v_y$  but will not change the gauge invariant quantity,  $C_v$ . Ideally we would like an alternative definition that completely fix the gauge. Such definition would, thus, determine which state should be identified with  $\mathbf{Q}_A$ . In this scenario, the sign of  $v_xv_y$  will be fixed by the gauge choice while the sign of  $m$  could be read out directly from the band structure and the symmetry of the Bloch waves for  $\mathbf{p} = 0$ .

We can achieve exactly this if we view our system with space group cm (for the gapped cones) and cmm (for the gapless cones) as derived by the  $\mathcal{C}_3$  symmetry breaking in a system with space group p3m1 (gapped cones) and p6m (gapless cones). In our particular case, the symmetry breaking comes from the silicon anisotropy and the elongated shape of the optical cavities. For the  $\mathcal{C}_3$  symmetric case, we will use the  $\mathcal{C}_3$  symmetry to fix the gauge and identify a robust feature to identify the normal mode  $\mathbf{Q}_A$ . Afterwards, in the symmetry broken case, we will appeal to a continuity argument to find the valley Chern number, see below.

The scenario with  $\mathcal{C}_3$  symmetry is discussed in detail in [14]. In this case, we recover Eq. (F9) with  $v = v_x = v_y$  and  $m', v_0 = 0$  if: (i) The quasi-momentum is counted off from the high-symmetry point  $\mathbf{K}$ . (ii) We identify the Bloch waves  $\mathbf{Q}_{A/B}(\mathbf{r})$  with eigenstates of the  $\mathcal{C}_3$  rotations with quasi-angular momentum  $m_c$  about the  $\mathcal{C}_6$  rotocenter of the original  $\mathcal{C}_{6v}$  symmetric design (the center of the snowflakes),  $m_c = -\sigma_z$ . (iii) We fix their phases to fulfill Eq. (F4) [14]. By requiring  $m_c = -\sigma_z$  we have fixed the sign of  $v_xv_y$  to be positive, thereby, there is no further ambiguity in the sign of  $m$  which now determines the valley Chern number,  $C_v = -\text{sign}(m)/2$ . For our particular geometry it is useful to keep in mind that the p3m1 has three rotocenters. In our geometry, the two additional rotocenters lie at the centers of the upward and downward-pointing triangles. The Bloch waves  $\mathbf{Q}_{A/B}(\mathbf{r})$  are simultaneous eigenstates of all rotations about any of the three rotocenters. The quasi-angular momentum  $m_{d/u}$  for the rotations about the center of the downward/upward-pointing triangles is [14]

$$m_{d/u} = (m_c \pm 1 + 1) \bmod 3 - 1. \quad (\text{F18})$$

For the Bloch wave  $\mathbf{Q}_A(\mathbf{r})$  we have  $m_d = 0$ , which means that it displays a breathing motion in the downward-pointing triangles. Likewise, the mode  $\mathbf{Q}_B(\mathbf{r})$  displays a breathing motion in the upper triangle.

Once the perturbation breaking the  $\mathcal{C}_3$  symmetry is introduced the Bloch waves  $\mathbf{Q}_{A/B}(\mathbf{r})$  are not anymore exact eigenstates of the  $\mathcal{C}_3$  rotations, nevertheless, the breathing motion is still clearly visible, cf. Fig. 1 (e-f). This allows us to identify the Bloch wave in Fig 1(f) (breathing motion in the downward-pointing triangles) with  $\mathbf{Q}_A(\mathbf{r})$  with the expectation that the product  $v_xv_y$  will be positive (the velocities should remain similar as in the  $\mathcal{C}_3$  symmetric limit,  $v_x, v_y \sim v$ ). Moreover, from the band structure Fig. 1(d) we see that the mass  $m$  is positive. We can conclude that the valley Chern number is  $C_v = -1/2$  for domain 1, cf. Eq. (F16).

### Derivation of the Dirac equation in a system combining domain 1 and domain 2

If the parameters of Eq. (F9) for domain 1 are known one can easily find the parameters for domain 2 (which is the mirror image of domain 1 in the  $zx$  plane) by transforming Eq. (F9) under the mirror symmetry  $M_y$ . Using Eqs. (F5) and (F6), we see that  $v_0$ ,  $v_x$ , and  $v_y$  remain the same in the two domains while  $m$  and  $m'$  change sign. Thus, the valley Chern number, cf. Eq. (F16), changes sign in domain 2,  $C_v = 1/2$ .

In a system combining both domain 1 and domain 2 we assume that a normal mode  $\mathbf{Q}_n(\mathbf{r})$  can be obtained by multiplying the Bloch waves Eq. (F3) for  $\mathbf{p} = 0$  by a smooth envelope,

$$\mathbf{Q}_n(\mathbf{r}) = \psi_{n,A}(\mathbf{r})\mathbf{Q}_A(\mathbf{r}) + \psi_{n,B}(\mathbf{r})\mathbf{Q}_B(\mathbf{r}). \quad (\text{F19})$$

This leads to the time-independent Schroedinger equation

$$\Omega_n \psi_n(\mathbf{r}) = \hat{H}_D \psi_n(\mathbf{r}), \quad (\text{F20})$$

where  $\psi_n(\mathbf{r})$  groups the smooth envelopes in a vector,  $\psi_n(\mathbf{r}) = (\psi_{n,A}(\mathbf{r}), \psi_{n,B}(\mathbf{r}))$ , and  $\hat{H}_D$  is the Dirac Hamiltonian Eq. (1) of the Main Text

$$\hat{H}_D = \bar{\Omega} + (v_0 + v_x \hat{\sigma}_x) \hat{p}_x + v_y \hat{\sigma}_y \hat{p}_y + \{\Theta(\hat{\mathbf{r}}), (m + m' \hat{p}_x)\} \hat{\sigma}_z. \quad (\text{F21})$$

Here  $\Theta(\mathbf{r}) = 1/2$  ( $\Theta(\mathbf{r}) = -1/2$ ) in domain 1 (2). We note that, here, position and quasi-momentum are non-commuting operators, thus, requiring the introduction of the anti-commutator  $\{, \}$  to make sure that the Hamiltonian is hermitian.

### Solution of the Dirac equation for a strip configuration

Next, we look for gapless eigenstates of Hamiltonian Eq. (F21) in the presence of translationally invariant domain walls. In this scenario, the quasi-momentum in the translationally invariant direction is a conserved quantity and the smooth envelope depends only on the coordinate transverse to the domain wall.

*Edge states for a horizontal strip.*

For a horizontal strip, the displacement field for smooth envelope Bloch waves takes the form

$$\mathbf{Q}_{p_x}(\mathbf{r}) = \psi_{A,p_x}(y)e^{ip_x x}\mathbf{Q}_A(\mathbf{r}) + \psi_{B,p_x}(y)e^{ip_x x}\mathbf{Q}_B(\mathbf{r}). \quad (\text{F22})$$

This results in a Hamiltonian of the form

$$\hat{H}_D = \bar{\Omega} + (v_0 + v_x \hat{\sigma}_x)p_x - iv_y \hat{\sigma}_y \frac{d}{dy} + 2\Theta(y)(m + m'p_x)\hat{\sigma}_z. \quad (\text{F23})$$

We are interested in the same configuration as in Fig 1(g) of the Main Text where domain 1 (domain 2) is in the lower-half (upper-half) plane. This choice corresponds to  $\Theta(y) = 1/2$  for  $y < 0$ , and  $\Theta(y) = -1/2$  otherwise. Until now we have assumed  $m > 0$ . We note that if we keep  $\Theta(y)$  fixed, and changing the sign of both  $m$  and  $m'$  describes a scenario where the two domains are swapped. In the following, we want to compare these two scenarios. For this purpose, we look for gapless edge eigenstates of the Hamiltonian Eq. (F23) without committing on the sign of  $m$  and  $m'$ . We find

$$\psi_{p_x}(y) = e^{-|(m+m'p_x)y/v_y|} \begin{pmatrix} 1 \\ \text{sign}(v_y m) \end{pmatrix}, \quad \Omega_{p_x} = \bar{\Omega} + (\text{sign}(v_y m)v_x + v_0)p_x. \quad (\text{F24})$$

This solution is valid for  $|m| > |m'p_x|$  (within the limit of validity of the linear expansion that underlies the Dirac equation). In the following, we also assume that  $|v_x| > |v_0|$  (in the scenario where this condition is violated the Dirac cones are of type II and the mass term does not lead to a global band gap.) From Eq. (F24) we see that, as expected, the propagation direction changes when the domains are swapped according to the bulk boundary correspondence [46]. More precisely, the edge state is a right mover if domain 1 is in the lower-half plane (for  $m > 0$ ,  $v_x v_y > 0$ ). Vice versa, it is a left mover if domain 1 is in the upper-half plane (for  $m < 0$ ,  $v_x v_y > 0$ ). This is consistent with the bulk-boundary correspondence because the valley Chern number  $C_v$  is  $-1/2$  in domain 1 and  $1/2$  in domain 2 and, thus, the edge state is a right (left) mover if the Chern number increases (decreases) by one across the domain wall. This is also in agreement with our FEM simulations, cf. Fig1(i, left panel) of the Main Text where the Dirac cone close to the  $\vec{K}$ -point which has positive quasi-momentum  $k_x$  in the first Brillouin zone of the bulk has negative quasi-momentum in the first Brillouin zone of a horizontal strip.

Until now, we have discussed general features of the Valley Hall effect that are not unique to our setting with broken  $\mathcal{C}_3$  symmetry. Eq. (F24) predicts also other more surprising features that are unique to our setting. Most remarkably, the speed  $|v_x + \text{sign}(m)v_0|$  changes if the two domains are swapped (changing the sign of  $m$ .) Moreover, the localization length of the edge state depends on the longitudinal quasi-momentum  $p_x$ . Both these features are confirmed in FEM simulations of a strip with a horizontal domain wall.

*Edge states for a slanted strip.*

Next, we calculate the solution when the domain wall is along the line  $\tilde{y} = -y/2 + \sqrt{3}x/2 = 0$  ( $240^\circ$  strip). In this scenario, it is convenient to change to a rotated frame with coordinates  $\tilde{y}$  (transverse to the domain wall) and  $\tilde{x} = -x/2 - \sqrt{3}y/2$  (longitudinal to the domain wall). In this case, the conserved quasi-momentum is  $p_{\tilde{x}}$  (in the direction  $\tilde{x}$ ) and the envelope is a function of  $\tilde{y}$ ,  $\psi_{p_{\tilde{x}}}(\tilde{y})$ . The Dirac Hamiltonian in terms of the rotated quasi-momenta and Pauli matrices,

$$\begin{aligned} p_x &= -p_{\tilde{x}}/2 + \sqrt{3}p_{\tilde{y}}/2, & p_y &= -p_{\tilde{y}}/2 - \sqrt{3}p_{\tilde{x}}/2, \\ \sigma_x &= -\sigma_{\tilde{x}}/2 + \sqrt{3}\sigma_{\tilde{y}}/2, & \sigma_y &= -\sigma_{\tilde{y}}/2 - \sqrt{3}\sigma_{\tilde{x}}/2, \end{aligned}$$

reads

$$\hat{H}_D = -i\partial_{\tilde{y}}(h'_0 + h'_{\tilde{x}}\sigma_{\tilde{x}} + h'_{\tilde{y}}\sigma_{\tilde{y}}) + \{-i\partial_{\tilde{y}}, \Theta(\tilde{y})\}h'_z\hat{\sigma}_z + h_0 + h_{\tilde{x}}\sigma_{\tilde{x}} + h_{\tilde{y}}\sigma_{\tilde{y}} + 2\Theta(\tilde{y})h_z\sigma_z \quad (\text{F25})$$

where

$$\begin{aligned} h'_0 &= \frac{\sqrt{3}}{2}v_0, & h'_{\tilde{x}} &= \frac{\sqrt{3}}{4}(v_y - v_x), & h'_{\tilde{y}} &= \frac{1}{4}(v_y + 3v_x), & h'_z &= \frac{\sqrt{3}}{2}m' \\ h_0 &= \bar{\Omega} - \frac{v_0}{2}p_{\tilde{x}}, & h_{\tilde{x}} &= \frac{1}{4}(v_x + 3v_y)p_{\tilde{x}}, & h_{\tilde{y}} &= \frac{\sqrt{3}}{4}(v_y - v_x)p_{\tilde{x}}, & h_z &= m - \frac{1}{2}m'p_{\tilde{x}}. \end{aligned}$$

In this case, to solve the Dirac equation (F20) with the Dirac Hamiltonian in the more general form Eq. (F25) we have to use the ansatz,

$$\psi_{p_{\tilde{x}}}(\tilde{y}) = (1 + i\epsilon\Theta(\tilde{y}))e^{-|\tilde{y}|/\xi + i\Xi\tilde{y}} \begin{pmatrix} 1 \\ b \end{pmatrix}. \quad (\text{F26})$$

Compared to Eq. (F24) this more general ansatz allows for oscillations of the wave function with period  $2\pi/\Xi$ . By plugging the ansatz Eq. (F26) into the Dirac equation (F20), we find three types of terms: (i) terms containing a delta function, (ii) terms in the form  $M_i\Theta(\tilde{y})\psi_{p_{\tilde{x}}}(\tilde{y})$  where  $M_i$  are matrices independent of  $\tilde{y}$ , and (iii) terms that depends on  $\tilde{y}$  only via the wave function  $\psi_{p_{\tilde{x}}}(\tilde{y})$ . By isolating the terms proportional to  $\delta(\tilde{y})$  and requiring their sum to be zero, we find the equation

$$[ih'_z\sigma_z + \epsilon(h'_0 + h'_{\tilde{x}}\sigma_{\tilde{x}} + h'_{\tilde{y}}\sigma_{\tilde{y}})] \begin{pmatrix} 1 \\ b \end{pmatrix} = 0. \quad (\text{F27})$$

It has a solution if

$$\det [ih'_z\sigma_z + \epsilon(h'_0 + h'_{\tilde{x}}\sigma_{\tilde{x}} + h'_{\tilde{y}}\sigma_{\tilde{y}})] = 0. \quad (\text{F28})$$

One immediately finds two possible solutions

$$\epsilon_{\pm} = \pm \frac{h'_z}{\sqrt{h_{\tilde{x}}'^2 + h_{\tilde{y}}'^2 - h_0'^2}}. \quad (\text{F29})$$

The corresponding  $b$  is

$$b_{\pm} = -\frac{h'_0 h'_{\tilde{x}} \mp \sqrt{h_{\tilde{x}}'^2 + h_{\tilde{y}}'^2 - h_0'^2} h'_{\tilde{y}} + i(h'_0 h'_{\tilde{y}} \pm \sqrt{h_{\tilde{x}}'^2 + h_{\tilde{y}}'^2 - h_0'^2} h'_{\tilde{x}})}{h_{\tilde{x}}'^2 + h_{\tilde{y}}'^2}. \quad (\text{F30})$$

Note that  $|b_{\pm}| = 1$  and, thus, the vectors  $(1, b_{\pm})^T$  lie on the equator of the Bloch sphere. Next, we require that the sum of the terms in the form  $\propto \Theta(\tilde{y})\psi_{p_{\tilde{x}}}(\tilde{y})$  is zero. We find the equation

$$[\xi(h_z + h'_z\Xi)\sigma_z + i(h'_0 + h'_{\tilde{x}}\sigma_{\tilde{x}} + h'_{\tilde{y}}\sigma_{\tilde{y}})] \begin{pmatrix} 1 \\ b \end{pmatrix}. \quad (\text{F31})$$

where  $b$  should be equal either to  $b_+$  or  $b_-$ . By requiring that the determinant is zero we find

$$\xi = \frac{1}{|h_z + h'_z\Xi|} (h_{\tilde{x}}'^2 + h_{\tilde{y}}'^2 - h_0'^2)^{1/2}. \quad (\text{F32})$$

By solving for  $b$  we find  $b = b_+$  ( $b = b_-$ ) if  $h_z + h'_z\Xi < 0$  ( $h_z + h'_z\Xi > 0$ ) independent of  $\Xi$ . Next, we need to require that the sum of the terms in the form  $\propto \psi_{p_{\tilde{x}}}(\tilde{y})$  is zero. We find the equation

$$(i\tilde{h}_z\sigma_z + \tilde{h}_{\tilde{x}}\sigma_{\tilde{x}} + \tilde{h}_{\tilde{y}}\sigma_{\tilde{y}} + \tilde{h}_0) \begin{pmatrix} 1 \\ b \end{pmatrix} = 0, \quad (\text{F33})$$

where

$$\tilde{h}_{\tilde{x}} = h_{\tilde{x}} + \Xi h'_{\tilde{x}}, \quad \tilde{h}_{\tilde{y}} = h_{\tilde{y}} + \Xi h'_{\tilde{y}}, \quad \tilde{h}_z = \frac{|h_z + h'_z\Xi|}{(h_{\tilde{x}}'^2 + h_{\tilde{y}}'^2 - h_0'^2)^{1/2}} h'_z, \quad \tilde{h}_0 = h_0 + \Xi h'_0 - \Omega_{p_{\tilde{x}}}. \quad (\text{F34})$$

To solve this it is convenient to define

$$\tilde{\phi} = \arg b, \quad \tilde{\sigma}_{\tilde{x}} = \cos \phi \sigma_{\tilde{x}} + \sin \phi \tilde{\sigma}_{\tilde{y}}, \quad \tilde{\sigma}_{\tilde{y}} = \cos \tilde{\phi} \sigma_{\tilde{y}} - \sin \tilde{\phi} \tilde{\sigma}_{\tilde{x}}. \quad (\text{F35})$$

and rewrite the equation in terms of the Pauli matrices  $\tilde{\sigma}_{\tilde{x}}$  and  $\tilde{\sigma}_{\tilde{y}}$ ,

$$\left( i\tilde{h}_z\sigma_z + (\cos\tilde{\phi}\tilde{h}_{\tilde{x}} + \sin\tilde{\phi}\tilde{h}_{\tilde{y}})\tilde{\sigma}_{\tilde{x}} + (\cos\tilde{\phi}\tilde{h}_{\tilde{y}} - \sin\tilde{\phi}\tilde{h}_{\tilde{x}})\tilde{\sigma}_{\tilde{y}} + \tilde{h}_0 \right) \begin{pmatrix} 1 \\ b \end{pmatrix} = 0. \quad (\text{F36})$$

From Eq. (F30), we can read out

$$\cos\tilde{\phi} = -\frac{h'_0 h'_{\tilde{x}} \pm \sqrt{h_{\tilde{x}}'^2 + h_{\tilde{y}}'^2 - h_0'^2 h_{\tilde{y}}'}}{h_{\tilde{x}}'^2 + h_{\tilde{y}}'^2}, \quad \sin\tilde{\phi} = -\frac{h'_0 h'_{\tilde{y}} \mp \sqrt{h_{\tilde{x}}'^2 + h_{\tilde{y}}'^2 - h_0'^2 h_{\tilde{x}}'}}{h_{\tilde{x}}'^2 + h_{\tilde{y}}'^2}. \quad (\text{F37})$$

We note that  $\tilde{\phi}$  is independent of  $\Xi$  and  $p_x$  and that by construction

$$\tilde{\sigma}_{\tilde{x}} \begin{pmatrix} 1 \\ b \end{pmatrix} = \begin{pmatrix} 1 \\ b \end{pmatrix}, \quad \sigma_z \begin{pmatrix} 1 \\ b \end{pmatrix} = i\tilde{\sigma}_{\tilde{y}} \begin{pmatrix} 1 \\ b \end{pmatrix} = \begin{pmatrix} 1 \\ -b \end{pmatrix}. \quad (\text{F38})$$

Plugging the above relations into Eq. (F36), we immediately find

$$\tilde{h}_z - \tilde{h}_{\tilde{y}} \cos\tilde{\phi} + \tilde{h}_{\tilde{x}} \sin\tilde{\phi} = 0, \quad \tilde{h}_{\tilde{x}} \cos\tilde{\phi} + \tilde{h}_{\tilde{y}} \sin\tilde{\phi} + \tilde{h}_0 = 0. \quad (\text{F39})$$

From the second equation we find

$$\Omega_{p_{\tilde{x}}} = h_0 + \Xi h'_0 + (h_{\tilde{x}} + \Xi h'_{\tilde{x}}) \cos\tilde{\phi} + (h_{\tilde{y}} + \Xi h'_{\tilde{y}}) \sin\tilde{\phi} \quad (\text{F40})$$

where  $\Xi$  is obtained by solving the first equation (which is a simple linear equation). The full expression for  $\Xi$  and  $\bar{\Omega}$  is very cumbersome and does not give much physical insight and, thus, we omit it here. Instead, it is interesting to comment on its leading order expansion in  $m'/\bar{v}, v_0/\bar{v}, \delta v/\bar{v}$  ( $\bar{v} = (v_x + v_y)/2, \delta v = v_x - v_y$ ),

$$\Xi \approx \frac{\sqrt{3}m}{2\bar{v}} \frac{m'}{\bar{v}} + \frac{\sqrt{3}}{2} \left( -\text{sign}(m\bar{v}) \frac{v_0}{\bar{v}} + \frac{\delta v}{\bar{v}} \right) p_x, \quad (\text{F41})$$

$$\Omega_{p_{\tilde{x}}} \approx \bar{\Omega} + \bar{v} \left( \text{sign}(m\bar{v}) - \frac{v_0}{2\bar{v}} - \text{sign}(m\bar{v}) \frac{\delta v}{4\bar{v}} \right) p_x. \quad (\text{F42})$$

From this expression we see that again the edge state (for the valley close to the  $\vec{K}$  point) is a right mover if the domain 1 is in the lower  $\tilde{y}$ -plane (for  $m > 0$ ). Also in this case (as for the horizontal domain wall) the speed changes if the two domains are exchanged. Compared to the horizontal domain wall, the edge state amplitude does not only decay away from the domain wall but it also displays oscillations with period  $2\pi/\Xi$ .

### Appendix G: Effect of Anisotropic Material Properties of Silicon

The Silicon crystal structure has a cubic primitive lattice, which leads to anisotropic material properties, and thus, the phononic band structures of our phononic crystal devices depend on the orientation of alignment during fabrication with respect to the Silicon crystal. The surface plane of the silicon wafer we used is parallel to the (001) crystal plane of Silicon. The alignment co-ordinate axes ( $x', y', z'$ ) during fabrication are oriented to the axes ([100], [010], [001]) of the Silicon wafer, cf. Fig 5c. Our FEM simulations take fully into account the anisotropy using an appropriate anisotropic elastic tensor [52]. In the presence of discrete translational symmetry, we may express the solutions to the acoustic wave equation as Bloch modes and numerically solve for the phononic band structure with an FEM solver [47]. Periodic boundary conditions are used to solve for the desired number of bands at any desired point within the Brillouin zone (BZ). The simulated phononic band structures for the two-dimensional snowflake unit cell are shown in Fig. 5f and g. We investigate the role of anisotropic material properties on the Dirac band dispersion. This is done by comparing the two-dimensional snowflake unit cell phononic band structure without (see Fig 5d) and with (see Fig 5e) circular photonic crystal holes for the two cases of isotropic (red solid lines) and anisotropic (blue solid lines) Silicon elasticity tensors. We notice that the Dirac bands for snowflakes without optical cavity holes (see Fig 5f) are significantly distorted for the anisotropic silicon elasticity tensor. Therefore, the small circular photonic crystal holes counter the distortion of Dirac bands by the anisotropic silicon (see Fig 5g).

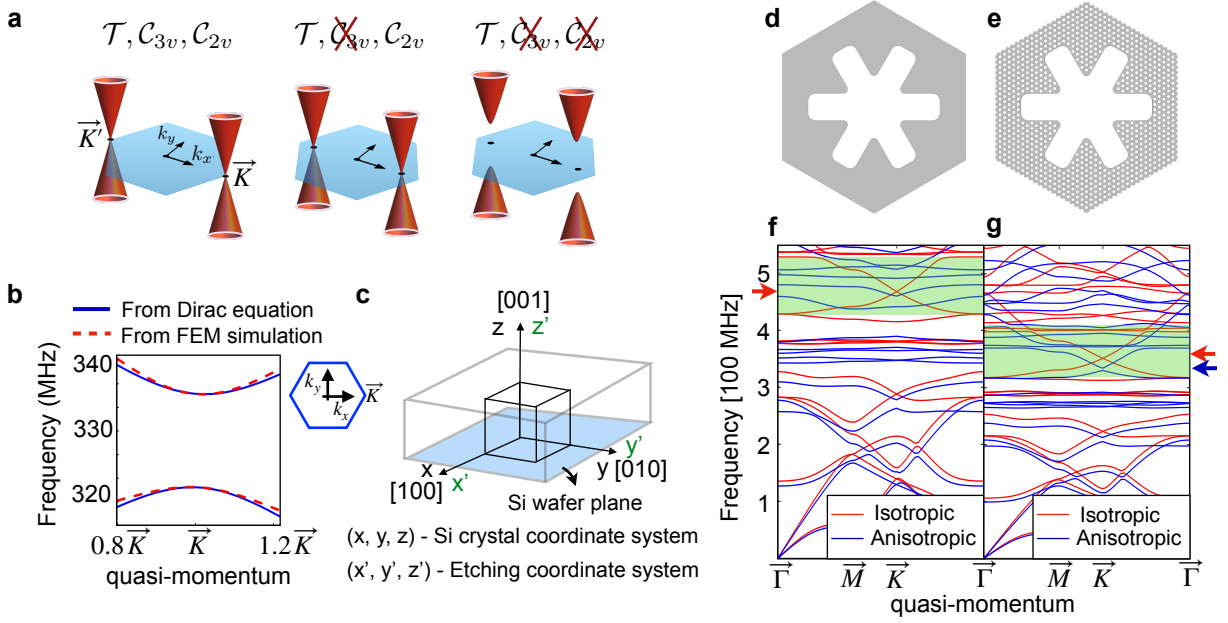


FIG. 5. **Effect of symmetries and anisotropic material properties of Silicon on the Dirac band dispersion.** **a**, Effects of different symmetries on the Dirac cones. Dirac cones are displaced from the  $K$  point when the  $D_{6v}$  symmetry (60-degree rotations and mirror symmetry) is broken. The degenerate cones split up when the  $D_{2v}$  symmetry is also broken. **b**, Comparison of the dispersion for the gapped Dirac cones, calculated from FEM simulations and the Dirac equation. **c**, The  $(x', y', z')$  axes of the fabricated devices are oriented with the  $[100]$ ,  $[010]$  and  $[001]$  planes of the Silicon cubic crystal, respectively. **d** and **e**, Unit cell geometry of the snowflake crystal in the presence or absence of the circular photonic crystal holes. **f** and **g**, the simulated phononic band structure with isotropic Silicon material properties and anisotropic Silicon material properties, respectively. The arrows indicate the Dirac cone frequencies. The Dirac cones are significantly distorted for the snowflake crystals without photonic crystal holes (**d** and **f**), compared to the one with photonic crystal holes (**e** and **g**).

## Appendix H: Optical readout of the thermal mechanical power spectrum

We measure the local thermal power spectrum of the mechanical modes in the bulk and domain wall regions. Readout of the mechanics is performed by observing the transduced sidebands in the optical cavity spectrum. We strongly drive an optical cavity at a blue-detuning of  $\bar{\Omega}$ , corresponding to the middle of the mechanical bulk band gap. In the frame rotating with the laser frequency  $\omega_L$ , the optical cavity (annihilation operator  $a$ ) interacting with the mechanical normal modes (annihilation operator  $b_n$  for the  $n$ -th mode) is described by the set of coupled Langevin equations,

$$\begin{aligned} \dot{a} &= \left(i\Delta - \frac{\kappa_t}{2}\right) a + i \sum_n g_{0n} a (b_n + b_n^\dagger) + \sqrt{\frac{\kappa_e}{2}} a_{in} \\ \dot{b}_n &= \left(-i\Omega_n - \frac{\Gamma_n}{2}\right) b_n + i g_{0n} a^\dagger a + \sqrt{\Gamma_n} b_{in,n} \end{aligned} \quad (\text{H1})$$

Here,  $\Delta = \omega_L - \omega_{cav} = \bar{\Omega}$  is the detuning and  $\kappa_t = \kappa_i + \kappa_e$  is the total optical decay rate. (We have a double-sided fiber taper coupling, because of which we observe only 50% of the output photons from the cavity.) The input phonon noise annihilation operator  $b_{in,n}$  represents the interaction of the mechanical system with the thermal bath. The optical noise is negligible. The mechanical decay rates  $\Gamma_n$  are almost constant,  $\Gamma_n \approx 200\text{kHz}$ , and we do not seek to model them. On the other hand, we determine the mechanical eigenfrequencies  $\Omega_n$  and the single-photon optomechanical coupling rates  $g_{0n}$  combining FEM simulation of a strip configuration to scattering matrix calculations, see App. I.

We linearize the equations of motion about the static equilibrium [1], and set  $a = \alpha + \delta a e^{i\theta}$ , where  $\alpha = |\alpha| e^{i\theta}$  ( $|\alpha|^2$

is the number of intra-cavity photons), and  $b_n = \beta_n + \delta b_n$ , with

$$\beta_n = \frac{i g_{0n} |\alpha|^2}{i \Omega_n + \Gamma_n/2} \approx \frac{g_{0n} |\alpha|^2}{\Omega_n} \quad (\text{H2})$$

$$\alpha = \frac{-\sqrt{\kappa_e/2} a_{in}}{i \Delta - \kappa_t/2 + i \sum_n g_{0n} (\beta_n + \beta_n^*)} \approx \frac{-\sqrt{\kappa_e/2} a_{in}}{i \Delta - \kappa_t/2 + 2i |\alpha|^2 \sum_n g_{0n}^2 / \Omega_n} \approx \frac{-\sqrt{\kappa_e/2} a_{in}}{i \Delta - \kappa_t/2} \quad (\text{H3})$$

Here, we have used  $\Omega_j \gg \Gamma_j$  and  $\kappa_t \gg |\alpha|^2 \sum_n g_{0n}^2 / \Omega_n$ . Ignoring the nonlinear interaction, the resulting equation of motion is

$$\delta \dot{a} = \left( i \bar{\Delta} - \frac{\kappa_t}{2} \right) \delta a + i \sum_n g_{0n} |\alpha| (\delta b_n + \delta b_n^\dagger) \quad (\text{H4})$$

$$\delta \dot{b}_n = \left( -i \Omega_n - \frac{\Gamma_n}{2} \right) \delta b_n + i g_{0n} |\alpha| (\delta a + \delta a^\dagger) + \sqrt{\Gamma_n} b_{in,n} \quad (\text{H5})$$

Here,  $\bar{\Delta} = \Delta + \sum_n g_{0n} (\beta_n + \beta_n^*)$ . For the frequency domain operators defined by  $O[\omega] = \frac{1}{2\pi} \int_{-\infty}^{+\infty} d\omega e^{i\omega t} O(t)$  and  $O^\dagger[\omega] = \frac{1}{2\pi} \int_{-\infty}^{+\infty} d\omega e^{i\omega t} O^\dagger(t) = [O[-\omega]]^\dagger$ , the above equation can be recasted to the following linear system of algebraic equations

$$\delta a[\omega] = i |\alpha| \chi_{opt}[\omega] \sum_n g_{0n} (\delta b_n[\omega] + \delta b_n^\dagger[\omega]) \quad (\text{H6})$$

$$\chi_n^{-1}[\omega] \delta b_n[\omega] = \sqrt{\Gamma_n} b_{in,n}[\omega] - i |\alpha|^2 g_{0n} (\chi_{opt}[\omega] - \chi_{opt}^*[-\omega]) \sum_{n'} g_{0n'} (\delta b_{n'}[\omega] + \delta b_{n'}^\dagger[\omega]) \quad (\text{H7})$$

$$(\chi_n^{-1}[-\omega])^* \delta b_n^\dagger[\omega] = \sqrt{\Gamma_n} b_{in,n}^\dagger[\omega] - i |\alpha|^2 g_{0n} (\chi_{opt}[\omega] - \chi_{opt}^*[-\omega]) \sum_{n'} g_{0n'} (\delta b_{n'}[\omega] + \delta b_{n'}^\dagger[\omega]) \quad (\text{H8})$$

where  $\chi_n[\omega] = [\Gamma_n/2 - i(\omega - \Omega_n)]^{-1}$  and  $\chi_{opt}[\omega] = [\kappa_t/2 - i(\omega + \bar{\Delta})]^{-1}$  are the mechanical and optical susceptibilities, respectively, in the absence of optomechanical coupling. We can ignore the optical backaction on the mechanics because our experiment is in a regime of small optomechanical cooperativity. Thus,

$$\delta a[\omega] = i |\alpha| \chi_{opt}[\omega] \sum_n g_{0n} \sqrt{\Gamma_n} (\chi_n[\omega] b_{in,n}[\omega] + (\chi_n[-\omega])^* b_{in,n}^\dagger[\omega]) \quad (\text{H9})$$

The output from the cavity is obtained via the input-output relations as

$$a_{out}[\omega] = a_{in} - \sqrt{\frac{\kappa_e}{2}} (\alpha + \delta a[\omega] e^{i\theta}) \quad (\text{H10})$$

$$= a_{in} \frac{i \Delta - \kappa_i/2}{i \Delta - \kappa_t/2} + a_{in} \frac{\kappa_e/2}{i \Delta - \kappa_t/2} i \chi_{opt}[\omega] \sum_n g_{0n} \sqrt{\Gamma_n} (\chi_n[\omega] b_{in,n}[\omega] + (\chi_n[-\omega])^* b_{in,n}^\dagger[\omega]) = \bar{a}_{out} + \delta a_{out}[\omega] \quad (\text{H11})$$

In our detection scheme, the strong laser beats with the optical sidebands. This generates photo-current proportional to the cavity output amplitude quadrature  $I(t) = \delta a_{out}(t) + \delta a_{out}^\dagger(t)$ . The cavity output power spectrum density is given by

$$S_{II}[\omega] = \int_{-\infty}^{\infty} dt e^{i\omega t} \langle I(t) I(0) \rangle = 2\pi \int_{-\infty}^{\infty} d\omega' \langle I[\omega] I[\omega'] \rangle \quad (\text{H12})$$

For a thermal bath of average phonon occupancy  $n_b$ , the correlation of the noise operators are  $\langle b_{in,n}^\dagger[\omega] b_{in,k}[\omega'] \rangle = n_b / (2\pi) \delta(\omega + \omega') \delta_{n,k}$  and  $\langle b_{in,n}[\omega] b_{in,k}^\dagger[\omega'] \rangle = (n_b + 1) / (2\pi) \delta(\omega + \omega') \delta_{n,k}$ . At room temperature  $T = 300K$  and  $\Omega_n = 330\text{MHz}$ ,  $n_b \approx k_B T / \hbar \Omega_n \approx 18940$  phonons. The boson occupancy is practically identical for all the standing wave mechanical normal modes, and we also assume  $n_b + 1 \approx n_b$  for simplicity. For  $\omega \approx \bar{\Omega}$  and  $\Omega_n \gg \Gamma_n$ , we find

$$S_{II}[\omega] = \frac{\kappa_e}{2} |\alpha \chi_{opt}[\omega] - \alpha^* \chi_{opt}^*[-\omega]|^2 \sum_n \frac{g_{0n}^2 n_b \Gamma_n}{(\omega - \Omega_n)^2 + (\Gamma_n/2)^2} = \frac{\kappa_e}{2} |\alpha \chi_{opt}[\omega] - \alpha^* \chi_{opt}^*[-\omega]|^2 \sum_n G_n^2 S_{\text{mech},n}[\omega] \quad (\text{H13})$$

$$G_n = \frac{g_{0n}}{x_{zpf,n}}, \quad S_{\text{mech},n}[\omega] = \frac{x_{zpf,n}^2 n_b \Gamma_n}{(\omega - \Omega_n)^2 + (\Gamma_n/2)^2}, \quad (\text{H14})$$

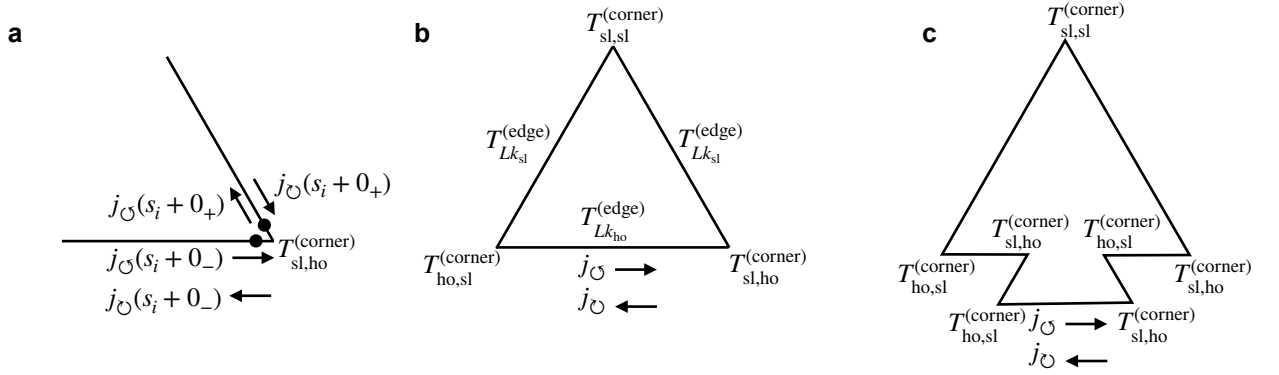


FIG. 6. **Schematic for the one-dimensional scattering matrix model.** **a**, Wave transport from the horizontal to the slanted waveguide through the corner is modelled with the transfer matrix  $T_{sl,ho}^{(corner)}$ . **b** (**c**), Modelling wave transport on the triangular (tree) topological mechanical cavities with different transfer matrices.

where  $x_{zpf,n}$  are the zero point fluctuations of the  $n$ -th mode.

So far the discussion has been generic and could refer to any cavity coupled to multiple mechanical modes. Next, we discuss the particular features that arise in the position resolved noise spectrum of our topological mechanical cavity because of the underlying topology. As discussed in the Main Text, the spectrum  $\Omega_j$  in the topological region is formed by a series of quasidegenerate doublets because of the suppression of backscattering (see the derivation below based on the scattering matrix approach). Each of these modes is a standing wave mode leading to a dependence of the optomechanical coupling on the optical cavity via its position (alternatively, as long as they are quasi-degenerate, they can be treated as running waves that are counterpropagating, leading to the same final result displayed below). Away from a corner, the domain wall hosting the topological mechanical cavity can be approximated as a 1D strip, and we expect the coupling to display a sinusoidal dependence on the cavity position,  $G_n(j) \propto \cos(k_l(\Omega_j)ja_m + \phi_j)$  where  $a_m$  is the length of strip unit cell,  $ja_m$  is the position of the  $j$ -th cavity and  $k_l(\Omega_n)$  is the quasi-momentum (which depends on the direction of the domain wall  $l$ ), see below for derivation. For quasidegenerate levels ( $\Omega_n \approx \Omega_{n+1}$ ), the couplings  $G_n(j)$  and  $G_{n+1}(j)$  will then be sinusoidal waves with the same period but a phase delay  $\phi_{n+1} - \phi_n \approx \pi/2$ . From Eq. (H13) we see that two quasidegenerate levels with a splitting  $\Omega_n - \Omega_{n+1}$ , much smaller than the mechanical decay rate  $\Gamma_n$ , give rise to a single mechanical couplings noise spectrum peak with a height proportional to the sum of the squares of their respective optomechanical couplings,

$$S_{II}[\Omega_n] \propto G_n^2 + G_{n+1}^2 \approx \cos^2(k_l(\Omega_n)ja_m + \phi_n) + \sin^2(k_l(\Omega_n)ja_m + \phi_n) \approx \text{const.} \quad (\text{H15})$$

Thus, we find that the peak height is the same for all cavities that are localized along the same edge of the polygonal-shaped domain wall and away from the corners. This feature is visible in the measured position resolved spectrum shown in Fig. 2(d) of the Main Text.

### Appendix I: Semi-analytical calculation of the spectra and optomechanical coupling for the mechanical topological cavity

Here, we discuss how we calculate the mechanical eigenfrequencies  $\Omega_j$  and optomechanical couplings  $g_{0j}$  used for the theoretical estimation of the power spectra of the mechanical topological cavity. A full FEM simulation of our device is not feasible due to the multiscale nature of our optomechanical crystal and the large system size. Instead, we adopt a hybrid approach where the spectra and optomechanical couplings are obtained from a scattering matrix calculation that uses the band structure and optomechanical couplings of strip configurations (with the two relevant orientations of the domain wall) obtained using FEM simulation as input.

#### Scattering matrix calculation of the spectrum $\Omega_n$

We model the topological mechanical cavity as a closed sequence of edge channels connected by scattering centers. We assume that away from the corners the mechanical waves propagate unimpeded as if they were flowing in an infinitely long edge channel. On the other hand, we describe the transmission across the corners phenomenologically

using the standard scattering-matrix approach. In the following, we assume that the domain 1 region has a polygonal form with sides in the horizontal direction (along the  $x$ -axis) or two different slanted directions ( $120^\circ$  or  $240^\circ$  from the  $x$ -axis). This general scenario applies to all the devices we have built.

We introduce the coordinate  $s$  that follows the domain wall length and denote as  $j_\circ(s)$  and  $j_\ominus(s)$  the mechanical edge current amplitudes circulating clockwise and anti-clockwise about domain 2, respectively (thus,  $|j_\circ(s)|^2$  and  $|j_\ominus(s)|^2$  are the corresponding mechanical energy fluxes).

Away from a corner, we assume that the mechanical wave propagates as in an infinitely long strip,

$$\begin{pmatrix} j_\circ(s + na_m) \\ j_\ominus(s + na_m) \end{pmatrix} = T_{na_mk_l(\Omega)}^{(\text{edge})} \begin{pmatrix} j_\circ(s) \\ j_\ominus(s) \end{pmatrix}, \quad T_\theta^{(\text{edge})} = \begin{pmatrix} e^{-i\theta} & 0 \\ 0 & e^{i\theta} \end{pmatrix}. \quad (\text{I1})$$

Here,  $n$  is an integer,  $a_m$  is the length of the strip unit cell,  $k_l(\Omega)$  is the quasi-momentum at frequency  $\Omega$  in the positive branch,  $k_l(\Omega) > 0$ , for an infinite strip. We note that the dispersion relation  $k_l(\Omega)$  depends on the domain wall orientation at  $s$ , horizontal ( $l = \text{ho}$ ) or slanted ( $l = \text{sl}$ ). The two slanted directions are equivalent because of the mirror symmetry about the  $yz$  plane. We note that  $j_\circ$  describes a wave propagating anticlockwise because  $dk_l(\Omega)/d\Omega < 0$  in the positive quasi-momentum branch, cf. Main Text Fig. 1.

Next, we denote as  $s_i$  the coordinate of a corner. The domain wall has different orientations  $l$  and  $r$  for  $s = s_i + 0_-$  (immediately before the corner) and  $s = s_i + 0_+$  (immediately after the corner), respectively. We connect the solutions at the two opposite sides of the corner using the appropriate transfer matrix,

$$\begin{pmatrix} j_\circ(s_i + 0_+) \\ j_\ominus(s_i + 0_+) \end{pmatrix} = T_{r,l}^{(\text{corner})} \begin{pmatrix} j_\circ(s_i + 0_-) \\ j_\ominus(s_i + 0_-) \end{pmatrix}, \quad T_{r,l}^{(\text{corner})}(r, t) = \frac{1}{t_{rl}} \begin{pmatrix} t_{rl} & -r_{rl}^* t_{rl}^* \\ -r_{rl} & 1 \end{pmatrix}. \quad (\text{I2})$$

Here,  $r_{rl}$  and  $t_{rl}$  are the complex reflection and transmission coefficients, respectively, and, thus,  $|r_{lr}|^2 + |t_{lr}|^2 = 1$ . The form of the T-matrix above reflects the symmetry under time-reversal and the conservation of the energy flux. By applying the mirror symmetry about the  $yz$  plane to Eq. (I2), one finds

$$T_{l,r}^{(\text{corner})} = \frac{1}{t_{rl}} \begin{pmatrix} t_{rl} & r_{rl} \\ r_{rl}^* t_{rl}^* & 1 \end{pmatrix}. \quad (\text{I3})$$

For the special case  $r = l = \text{sl}$ , combining the above equation with Eq. (I2) gives the constraint  $r_{\text{sl,sl}}^* t_{\text{sl,sl}} + t_{\text{sl,sl}}^* r_{\text{sl,sl}} = 0$ . Thus, we are left with five independent transfer matrix parameters:  $t_{\text{ho,sl}}$ ,  $r_{\text{ho,sl}}$  (two independent phases and one independent amplitude) and  $t_{\text{sl,sl}}$  (independent amplitude and phase.)

Using the building blocks Eqs. (I1,I2) and the symmetry constraint Eq. (I3) we can build a transfer matrix  $T_{\text{loop}}$  that evolves the current amplitude from a point  $s$  on a closed loop around the whole domain wall length. For example, for the triangle of side  $L$  we find the loop T-matrix

$$T_{\text{loop}} = T_{\text{ho,sl}}^{(\text{corner})} T_{Lk_{\text{sl}}}^{(\text{edge})} T_{\text{sl,sl}}^{(\text{corner})} T_{Lk_{\text{sl}}}^{(\text{edge})} T_{\text{sl,ho}}^{(\text{corner})} T_{Lk_{\text{ho}}}^{(\text{edge})} \quad (\text{I4})$$

The loop T-matrix allows to impose the appropriate periodic boundary conditions, requiring

$$\det(T_{\text{loop}} - \mathbb{1}) = 0. \quad (\text{I5})$$

This equations can then be solved to give the spectrum  $\Omega_n$  in terms of the transfer matrix parameters. Vice versa, when the spectrum is known, one can use the same equation to extract information about the transfer matrix parameters.

#### *Analytical calculation of the spectrum $\Omega_j$ in the absence of backscattering*

We note that in the limit of zero backscattering (corresponding to the special case  $r_{\text{sl,sl}} = r_{\text{ho,sl}} = 0$ ) the matrix  $T_{\text{loop}}$  is diagonal and as a consequence the spectrum is formed by degenerate doublets that solve the simple equation

$$L_{\text{sl}} k_{\text{sl}}(\Omega) + L_{\text{ho}} k_{\text{ho}}(\Omega) + N_{\text{sl,sl}} \arg(t_{\text{sl,sl}}) + N_{\text{sl,ho}} \arg(t_{\text{sl,ho}}) = n2\pi. \quad (\text{I6})$$

Here,  $L_{\text{sl}}$  ( $L_{\text{ho}}$ ) is the total length along slanted sides, and  $N_{\text{sl,sl}}$  ( $N_{\text{sl,ho}}$ ) is the number of corners connecting two slanted sides (a slanted and a horizontal side). Importantly, according to this formula (that assumes no backscattering) we expect the same spectrum for the two different tree-shaped cavity geometries. This is the tell-tale signature for the absence of backscattering (as a consequence of the topological nature of the transport) that we will be looking for in the experiment.

By deriving Eq. (I6) with respect to the frequency we find a simple expression for the free spectral range between two doublets

$$\Omega_{j+2} - \Omega_j \approx \frac{2\pi v_{sl} v_{ho}}{L_{sl} v_{ho} + L_{ho} v_{sl}}. \quad (\text{I7})$$

where  $v_{sl} = d\Omega/dk_{sl}$  ( $v_{ho} = d\Omega/dk_{ho}$ ) is the group velocity on a slanted (horizontal) side. Here, we have assumed that the transmission amplitudes  $t_{sl,sl}$  and  $t_{sl,ho}$  are frequency independent. We note that the assumption of constant scattering parameters clearly breaks down at the crossover region between the topological and trivial region (about the edge of the horizontal strip bandwidth) where the transmission across the slanted-horizontal corners  $t_{sl,ho}$  must go to zero. This is the reason for the mismatch between the measured and theoretical noise spectra in that region. We do not seek to model the crossover region.

### Calculation of the vacuum OM couplings $g_{0n}$

In this section we show how to estimate the vacuum optomechanical couplings  $\{g_{0n}\}$  for the normal modes  $\{\mathbf{Q}_n(\mathbf{r})\}$  of the topological mechanical cavity. By definition, this is the cavity shift by a displacement field with amplitude equal to the zero-point fluctuations. By requiring that the energy stored in the vibrations  $\Omega_j^2 \int_V |\mathbf{Q}_n(\mathbf{r})|^2 \rho(\mathbf{r}) d^3\mathbf{r}$  is equal to the zero point energy  $\hbar\Omega_j/2$  we find the normalization condition

$$\int_V |\mathbf{Q}_n(\mathbf{r})|^2 \rho(\mathbf{r}) d^3\mathbf{r} = \frac{\hbar}{2\Omega_n}. \quad (\text{I8})$$

The cavity shift  $g_{0j}$  is then given by the standard perturbative formulas  $g_{0n} = g_{0n}^{(\text{PE})} + g_{0n}^{(\text{Bnd})}$  with the moving boundary contributions and photoelastic contributions

$$g_{0n}^{(\text{Bnd})} = -\frac{\omega_0}{2} \frac{\int_A (\mathbf{Q}_n(\mathbf{r}) \cdot \mathbf{n}) ((\varepsilon(\mathbf{r}) - \varepsilon_0) |\mathbf{e}^{\parallel}(\mathbf{r})|^2 - (\varepsilon(\mathbf{r}) - \varepsilon_0)^{-1} |\mathbf{d}^{\perp}(\mathbf{r})|^2) dA}{\int_V |\mathbf{e}(\mathbf{r})|^2 \varepsilon(\mathbf{r}) d^3\mathbf{r}} \quad (\text{I9})$$

$$g_{0n}^{(\text{PE})} = -\frac{\omega_0}{2} \frac{\int_V \mathbf{e}(\mathbf{r}) \cdot \delta\varepsilon(\mathbf{r}) \cdot \mathbf{e}(\mathbf{r})}{\int_V |\mathbf{e}(\mathbf{r})|^2 \varepsilon(\mathbf{r}) d^3\mathbf{r}} \quad (\text{I10})$$

where  $\mathbf{e}(\mathbf{r})$  and  $\mathbf{d}(\mathbf{r})$  are the electric and the electric displacement fields in the cavity mode, respectively. Moreover,  $\varepsilon(\mathbf{r})$  is the permittivity, and the tensor  $\delta\varepsilon(\mathbf{r})$  is the local change of permittivity due to the strain. For the purpose of our discussion it is only important that the mapping between the displacement field  $\mathbf{Q}_n(\mathbf{r})$  and the tensor  $\delta\varepsilon(\mathbf{r})$  (via the strain tensor) is linear, see Ref. [53] for more details. Since the electric and the displacement fields are exponentially localized within a single triangular membrane, we can approximate the displacement field as

$$\mathbf{Q}_n(\mathbf{r}) \approx A_{n,i} e^{ik_l(\Omega)s} \mathbf{u}_{n,l,\Omega_n}(\mathbf{r}) + A_{n,i}^* e^{-ik_l(\Omega)s} \mathbf{u}_{n,l,\Omega_n}^*(\mathbf{r}), \quad (\text{I11})$$

where  $\exp[ik_l(\Omega)s] \mathbf{u}_{n,l,\Omega_n}(\mathbf{r})$  are the edge state Bloch waves for an infinite strip with the appropriate orientation. Thus,  $\mathbf{u}_{n,l,\Omega_n}(\mathbf{r})$  is a periodic function in the domain wall direction, e.g. it is periodic in  $x$  for  $l = ho$ , and is exponentially localized about the domain wall in the transverse direction. The complex amplitude  $A_{n,i}$  is assumed to be constant in the region of the cavity but its value, to be calculated using the scattering matrix approach and imposing the normalization condition Eq. (I8), may depend on the side of the polygon-shaped domain wall labeled by the second index  $i$ , see below.

Next, we define the vacuum 1D optomechanical coupling (per unit cell)  $g_{0,l}^{(1D)}(\Omega)$  (the quantity plotted in Fig. 2 of the Main Text) as the cavity shift in the presence of a 1D Bloch wave  $\mathbf{u}_{n,l,\Omega}(\mathbf{r})$  of amplitude set by the normalization condition

$$\int_U |\mathbf{u}_{n,l,\Omega}(\mathbf{r})|^2 \rho(\mathbf{r}) d^3\mathbf{r} = \frac{\hbar}{2\Omega_n}, \quad (\text{I12})$$

where  $U$  indicates the unit cell of the strip. This definition has the merit to be independent of the size of the system (length of the strip) and is, thus, suitable to be computed using finite element simulations. We note that we can fix the phase of  $\mathbf{u}_{n,l,\Omega}(\mathbf{r})$  by requiring that  $g_{0,l}^{(1D)}(\Omega)$  is real. Using this definition and substituting Eq. (I11) into Eq. (I9), we find

$$g_{0n}(s) = g_{0,l}^{(1D)}(\Omega_n) 2|A_{n,i}| \cos(k_l(\Omega)s + \arg(A_{n,i})) \quad (\text{I13})$$

where  $s$  is the position of the cavity. Thus, the task of calculating the optomechanical coupling reduces to the task of calculating the amplitude  $A_{n,i}$ . This is done by noting that using Eq. (I11), we can identify the amplitude of the clockwise and anti-clockwise mechanical energy fluxes with

$$j_{\circlearrowright}(s) = \left(v_l \frac{\hbar\Omega_n}{2a_m}\right)^{1/2} A_{n,i} e^{ik_l(\Omega)s}, \quad j_{\circlearrowleft}(s) = \left(v_l \frac{\hbar\Omega_n}{2a_m}\right)^{1/2} A_{n,i} e^{-ik_l(\Omega)s}, \quad (\text{I14})$$

respectively. Thus, we can calculate  $A_{n,i}$  from Eq. (I5) modulus a normalization factor (the global phase of the solution of Eq. (I5) does not have a physical meaning and is fixed by requiring that  $j_{\circlearrowright}(s) = j_{\circlearrowright}^*(s)$ . This is always possible because of the time-reversal symmetry). The normalization factor is fixed by Eq. (I8). Using Eq. (I11) and Eq. (I12), the latter constraint can be rewritten as

$$1 = \sum_i 2|A_{n,i}|^2 N_i, \quad (\text{I15})$$

where  $N_i$  is the length of the side  $i$  (in number of unit cells).

For the case of zero backscattering the flux  $|j_{\circlearrowright}(s)|$  is constant, cf. Eq. (I5). Thus, from Eq. (I14) and Eq. (I15) we find

$$|A_{n,\text{ho}}| = \left(\frac{a_m v_{\text{sl}}}{2(L_{\text{ho}} v_{\text{sl}} + L_{\text{sl}} v_{\text{ho}})}\right)^{1/2}, \quad |A_{n,\text{sl}}| = \left(\frac{v_{\text{ho}}}{v_{\text{sl}}}\right)^{1/2} |A_{n,\text{ho}}|. \quad (\text{I16})$$

where  $|A_{n,\text{ho}}|$  ( $|A_{n,\text{sl}}|$ ) is the amplitude on all horizontal (slanted) sides. We note that for a pair of degenerate solutions have the same amplitudes,  $|A_{n,1}| = |A_{n+1,1}|$ , while  $|\arg(A_{n,1}/A_{n+1,1})| = \pi/2$  to ensure that the two solutions are orthogonal.

It is interesting to estimate the typical amplitude of the zero-point and the thermal fluctuations in our topological cavity. For the zero point fluctuations we have [53]

$$x_{\text{zpf},n} = \text{Max}[\mathbf{Q}_n(\mathbf{r})]_V \approx |A_{n,\text{ho}}| \text{Max}[\mathbf{u}_{n,l,\Omega_n}(\mathbf{r})]_U \approx N^{-1/2} \text{Max}[\mathbf{u}_{n,l,\Omega_n}(\mathbf{r})]_U \quad (\text{I17})$$

We calculate the quantity  $\text{Max}[\mathbf{u}_{n,l,\Omega_n}(\mathbf{r})]_U$  using FEM simulations. It turns out that  $\text{Max}[\mathbf{u}_{n,l,\Omega_n}(\mathbf{r})]_U \sim 1\text{fm}$ . Taking into account that for our devices  $N \sim 100$  we find

$$x_{\text{zpf},n} \sim 0.1\text{fm}. \quad (\text{I18})$$

We can then readily find the typical amplitude of the thermal vibrations in our experiment to be

$$x_{\text{th}} \sim \sqrt{\frac{k_B T}{\hbar\Omega}} x_{\text{zpf},n} \sim 10\text{fm}. \quad (\text{I19})$$

### Fitting parameters

In calculating the spectrum  $\Omega_n$  and the corresponding optomechanical couplings  $g_{0n}$ , we have made the simplifying assumption that the propagation along the domain wall is similar as the propagation in an infinitely long domain wall and abruptly switch to the propagation in a domain wall with a different orientation after turning a sharp angle. This allows for a simple theoretical description but is not entirely realistic in the region close to the corners. A more realistic point of view is that Eq. (I1) is valid only away from the corners and Eq.(I2) describes the propagation across a finite region about the corners. In view of this physical interpretation, we replace in our calculation of the noise spectrum the lengths of the sides of the polygon-shaped domain wall with effective lengths that are determined using the total length of the domain wall as a fitting parameter and rescaling accordingly the single side lengths.

For the plots where we have assumed perfect transmission we take also the overall phase acquired by crossing the three corners (for the triangle  $\arg(t_{\text{sl,sl}} + 2t_{\text{sl,ho}})$ ) as a fitting parameter.

In addition we have used a uniform shift of the band structure as a fitting parameter. This is justified because, within the topological bandwidth of our devices, the main effect of a rescaling of the whole band structure by as little as  $\sim 1\%$  would be a uniform shift of the order of the free spectral range. This could be caused by any residual mismatch between the fabrication and the nominal parameters used for our FEM simulations. Indeed, we have observed a uniform shift of the band structure even post fabrication comparing measurement taken on the same device in different days. We attribute this drift, that tends to saturate after some time, to oxidation of the device surface.

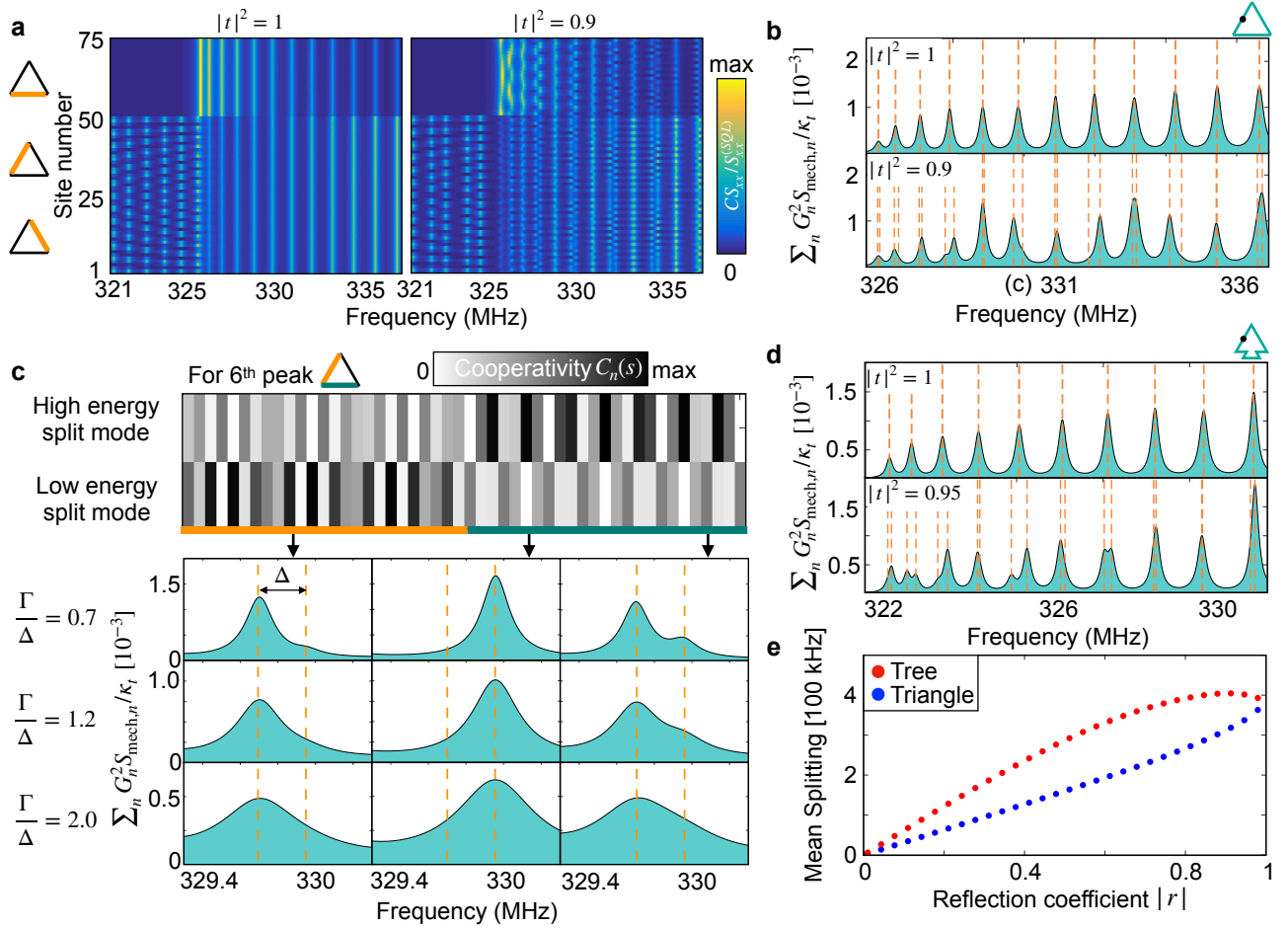


FIG. 7. **Signatures of backscattering on the spectrum.** **a**, Theoretically predicted spectra on all the sites of the triangular topological mechanical cavity (shown in the form of a density plot). For non-vanishing backscattering  $|t|^2 = 0.9$ , the spectra become position-dependent, i.e. they are no longer identical for all the sites on the slanted or the horizontal waveguide. **b** (d), Local spectrum for triangular (tree) topological mechanical cavity at the middle of the long slanted waveguide, in the absence and presence of small backscattering. The orange dashed lines indicate the eigenvalues. In the presence of small backscattering, the degenerate peaks are split and the amplitudes of the peaks are modulated. **c**, Intensity mode profile (displayed in terms of optomechanical cooperativity) of the two split modes of the 6<sup>th</sup> doublet peak for the triangular topological mechanical cavity. Resulting spectrum around this peak at different sites for small, intermediate and large values of mechanical damping  $\Gamma$ . **e**, Comparison of the mean splitting for the triangular and tree topological mechanical cavities. The splitting is larger for the tree cavity because it has more corners than the triangular cavity.

### Effect of finite backscattering on the spectrum

Here, we study the effect of backscattering on the NPSD. As discussed above in order to calculate the NSPD we first have to calculate the eigenfrequencies  $\Omega_n$  and the optomechanical couplings  $g_{0n}$  in the transfer matrix approach using Eqs. (I5,I15,I13). Then, we can plug these quantities into the general expression Eq. H13. For simplicity we always assume  $t_{\text{sl,sl}} = t_{\text{sl,ho}} = t$ .

Fig. 7(a) shows the triangle NPSD for  $|t|^2 = 0.9$  (right). For comparison, we also show the results calculated assuming perfect transmission,  $|t|^2 = 1$  (left).

In the presence of backscattering ( $|r|^2 \neq 0$ ), the underlying doublets  $\Omega_n$  and  $\Omega_{n+1}$  (indicated by orange lines in Fig 7 (b) and (d)) are split. The splitting averaged over all doublets as a function of  $|r|$  is plot in Fig. 7 (e). We note that the average splitting is always larger for the tree-shaped topological cavity than for the triangular cavity. This should be expected because of the larger number of corners acting as scattering centers for the tree geometry. The splitting of the underlying doublets changes the lineshape of the NPSD. The position dependence of the lineshape is governed by the ratio of the splitting and the decay rate and is studied for the 6-th peak in 7 (c). We note that for splittings  $\Delta$

similar to the decay rate  $\Gamma$  (top and center panel), we see either one or two peaks in the spectrum, depending on the position dependence of the intensity profiles of the two modes (via the position dependent optomechanical couplings, cf. Eq. (I13)) at the measurement location. On the other hand, in the regime of our experiment where the splitting  $\Delta$  is smaller than the decay rate  $\Gamma$ , there is always a single peak. In this regime the residual small splitting  $\Delta$  is revealed by what looks like a position dependent drift of the peak location.

### Appendix J: Calibration of frequency drift and normalization of NPSD spectra of the mechanical topological cavity

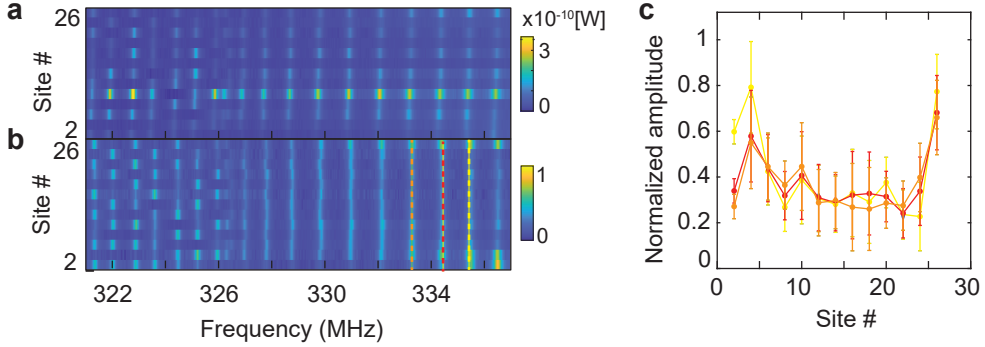


FIG. 8. **Calibration of frequency drift and normalization of NPSD spectra of the mechanical topological cavity** **a**, Density plot of the measured NPSD before frequency drift calibration amplitude normalization, as a function of frequency and read-out position along a slanted edge. **b**, Density plot of the same measured NPSD after frequency drift calibration and amplitude normalization. **c**, Normalized peak amplitudes versus measurement locations for 3 peaks, corresponding frequencies are indicated with dashed lines in **b**. Error bars correspond to the standard deviation of the 5 peak amplitudes used for the amplitudes normalization.

We have observed a uniform shift of the band structure during measurements comparing spectra taken on the same device on different days. We attribute this drift, that tends to saturate after some time, to surface oxidation of the silicon device. In addition, the total optical loss  $\kappa$ , external coupling efficiency  $\kappa_e/\kappa$ , as well as the total optical power delivered to each optical cavity during measurements are different, hence the amplitude of the optically transduced mechanical NPSD received on spectrum analyzer are different for each site. Therefore, we have applied spectra normalization, as discussed below, for the Main Text figures Fig.2 and Fig.3.

The frequency drift is calibrated using the two peaks between 323 MHz and 325 MHz. The frequency spectra of all the sites are shifted such that these two peaks align as well as possible with the corresponding two peaks at the (arbitrarily selected) reference site #26. To illustrate this procedure, the raw spectra are plotted in Fig. 8a; it can be seen that there is a drift in mechanical frequency to lower frequencies from site #26 to site #2. In Fig. 8b, the frequency drifts have been removed by the calibration.

The amplitudes of the measured spectra are also normalized. Essentially, there are differences in the intensities between measurements at different sites due to these sites being measured individually in succession, with different  $\kappa$ ,  $\kappa_e/\kappa$ , and total optical power delivered to the optical cavity during measurements. These spurious differences (that are not connected to the intrinsic physics of the device) are removed by calibration in the following manner. The five highest peaks in the grey low-frequency region (cf. Main Text Fig. 1i) are averaged, and the mean value is used to normalize each spectrum. The theoretical expectations for the NPSD as a function of frequency and read-out position on a slanted edge are plotted in Fig. 7a. Figure 8 shows the normalized peak amplitudes versus measurement location for 3 peaks. It can be seen that the normalized NPSD near the center of the slanted side of the triangle mechanical topological cavity are constant within error.

We remark briefly on why we have chosen our calibration procedure in this way. Our aim in this site-resolved measurement was to test experimentally whether the high-frequency region indeed harbors running wave modes that have little to no backscattering, as expected from the topological nature of the edge channels. Such modes would then show up with an intensity that is independent of position (in the idealized absence of changes of coupling strength between the measurements at different sites). In order to test this hypothesis without bias, we decided against normalizing the overall intensity based on peaks in this high-frequency region (because this could be viewed as enforcing at least an average tendency towards location-independent intensities). We rather took peaks in the

low-frequency region as a reference for the normalization. Since in that region we expect standing waves (due to backscattering at the ends of the edge), each individual frequency peak is already strongly location-dependent in its intensity. To avoid hampering the overall normalization by this fact, we averaged over the five highest peaks.

### Appendix K: Calibration of the optomechanical coupling rate

The optomechanical coupling of the between localized optical resonance and mechanical resonance can be estimated using two different methods. The first method, the increase in the mechanical linewidth of each mechanical mode can be fitted as a function of optical power to find the optomechanical coupling for each mode. However, the increased mechanical linewidth of our devices is on the order of few hundred Hz ( $\gamma_{\text{OM}} < 1$  kHz), even with large number of cavity photons ( $n_c \approx 10000$ ), which is small compared to the intrinsic mechanical linewidth ( $\gamma_i \approx 200$  kHz). The second method involves calibration of the optical powers and electronic detection system, and uses the fact that the transduced thermal Brownian motion of the mechanical resonator is proportional to  $g_{0n}^2$ .

To calibrate the detection efficiency of the setup we first measure the efficiency of transmission from laser to the input power of the dimpled fiber taper. These values are measured once when the optical components are connected and do not change. To measure the efficiency of dimpled fiber taper, the laser is tuned off-resonance from the optical mode (where the device optical transmission should be flat) and a continuous-wave signal of input power  $P_{\text{in}}$  is sent into input port of the dimpled fiber taper. The optical losses incurred in the path input port of taper to the device-under-test are accumulated into an efficiency factor  $\eta_{\text{taper}}$ . These losses are incurred twice in transmission to the output of the taper (loss in the input side of taper is assumed to be the same as output side), so a power of  $\eta_{\text{taper}}^2 P_{\text{in}}$  propagates out of output port of the taper. This signal is sent to a power meter (PM), and thus the coupling efficiency of taper is determined as  $\eta_{\text{taper}} = \sqrt{P_{\text{PM}}/P_{\text{in}}} = 51\%$ .

To calibrate the overall detection efficiency ( $\eta_{\text{det}}$ ), we must also determine the efficiency of the rest of the detection path and detector. This is accomplished by using the amplitude modulator to create optical sidebands detuned from the signal by the mechanical frequency while the laser is tuned off-resonance from the optical mode. The power  $P_{\text{cal}}$  in this sideband is calculated using  $V_{\pi}$  of EOM and  $\eta_{\text{taper}}$ . The photocurrent NPSD ( $S_{\text{pc}}[\omega]$ ) as transduced on the spectrum analyser is given by

$$S_{\text{pc}}[\omega] = S_{\text{dark}} + \frac{G_e^2}{R_L} S_{\text{SN}}^2 \left( 1 + \frac{\eta_{\text{det}} S_{\text{cal}}[\omega]}{\hbar\omega_o} \right), \quad (\text{K1})$$

where  $S_{\text{dark}}[\omega]$  is the electronic NPSD of the detector,  $S_{\text{SN}} = \sqrt{2\hbar\omega_o P_{\text{drive}}}$  is the optical shot-noise NPSD arising from driving optical power at optical frequency  $\omega_l$ , which lies an order of magnitude above the electronic noise, and  $S_{\text{cal}}$  is the NPSD of the signal, where  $\int_{-\infty}^{\infty} S_{\text{cal}}[\omega] \frac{d\omega}{2\pi} = \eta_{\text{taper}}^2 P_{\text{cal}}$ . The gain factor  $G_e$  represents the conversion from optical power to voltage while  $R_L$  is the input impedance of the spectrum analyser. The total noise floor  $S_{\text{noise}} = \frac{G_e^2}{R_L} S_{\text{SN}}^2 + S_{\text{dark}}$  is measured with the EOM drive turned off (no optical sidebands), while  $S_{\text{dark}}$  is measured independently with both signal and drive laser beams blocked (laser is blocked at BOA). The calibration tone (with NPSD  $S_{\text{cal}}[\omega]$ ) picks up losses in the optical setup (fibers, fiber unions), fast optical detector, and microwave cable, which are parametrized into  $\eta_{\text{det}}$ . The efficiency of the thermal vibration NPSD detection path is extracted as

$$\eta_{\text{det}} = \frac{\hbar\omega_o}{\eta_{\text{taper}}^2 P_{\text{cal}}} \int_{-\infty}^{\infty} \frac{S_{\text{pc}}[\omega] - S_{\text{noise}}}{S_{\text{noise}} - S_{\text{dark}}} \frac{d\omega}{2\pi} = 9.7\%. \quad (\text{K2})$$

In order to calibrate  $g_{0n}$ , the fiber taper is parked on the device-under-test, which is one of the center sites of slanted edge of a tree-shaped cavity geometry in this calibration. The optical drive laser is locked to a blue detuning (from the optical cavity resonance) of 340 MHz, and the optical drive power is tuned such that the same amount of power is received on the photodetector. With

$$S_{\text{pc}}[\omega] = S_{\text{dark}} + \frac{G_e^2}{R_L} S_{\text{SN}}^2 \left( 1 + \frac{\eta_{\text{det}} S_{\text{II}}[\omega]}{\hbar\omega_o} \right), \quad (\text{K3})$$

where  $S_{\text{II}}$  is the NPSD of optomechanically generated photons, given by Eq. H13. For the tree-shaped topological cavity, we get calibrated  $g_{0n}/2\pi = 2.56$  kHz for one peak (328.21 MHz) within topological bandwidth, which is in good agreement with the theoretically predicted value (Eq. I13) for the same peak,  $g_{0n}/2\pi = 2.25$  kHz. We note that this agreement implies that we are indeed observing thermal motion ( $S_{\text{II}}$  in Eq. H13 is calculated for the room temperature 300 K).

## Appendix L: Trivial waveguide design

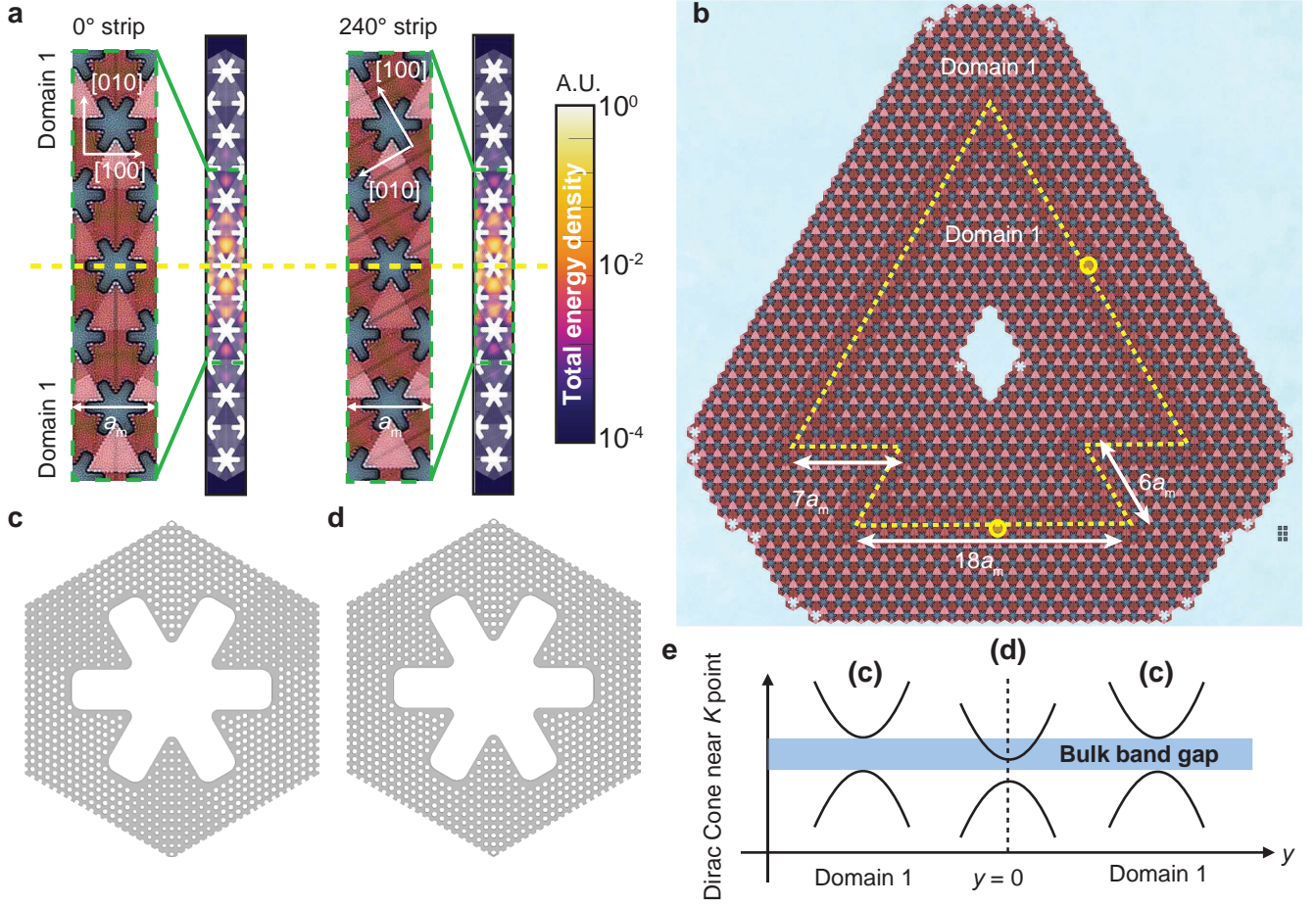


FIG. 9. **Trivial waveguide** **a**, Optical microscope images and simulated mechanical mode profiles of the strip unit cell for  $0^\circ$  (horizontal) or  $240^\circ$  (slanted) vs. the silicon [100] crystal orientation. A defect trivial waveguide is built by modifying the radius of the holes in the upward-pointing triangles near the center three snowflakes. **b**, Optical microscope image of the tree-shaped trival mechanical cavity. The dimensions are similar to that of topological mechanical cavity in Fig. 3(b) of Main Text. The center of trivial waveguide is indicated by dashed lines. Mechanical NPSD is measured at the horizontal and slanted edges of tree geometry as indicated by the yellow dots. **c**, Unit cell in domain 1. **d**, Unit cell of the center three snowflakes. **e**, The Dirac cone bands of center three snowflakes are tuned into the bulk band gap by changing the size of the circular holes in the upward-pointing triangles.

In this section, we describe the design of the trivial waveguide, which is used in Fig. 3 of Main Text to show the effects of backscattering at the sharp corners. The strip unit cell is built by locally tuning the upper band of the gapped Dirac cone of the central region to be inside of the bulk bandgap of the two-dimensional snowflake phononic crystal (see Fig. 9 (a) and (e)). Note that there is no band inversion in this strip unit cell at its center. Trivial waveguide is formed in the center three snowflakes by the upper band of the gapped Dirac cone, corresponding optical microscope images and simulated mechanical mode profiles of  $0^\circ$  and  $240^\circ$  of the strip unit cells vs. Silicon [100] are shown in Fig. 9(a). In the center three snowflake unit cells, the circular holes in the upward-pointing triangles (light red) are scaled smaller by a factor of 0.92 in comparison to the downward-pointing triangles (see Fig 9(d)). While in domain 1, circular holes in the upward-pointing triangles are scaled smaller by a factor of 0.78 (see Fig. 9(c)). Larger circular holes shifts the gapped Dirac cones lower in energy because of the decreasing stiffness (see Fig 9(e)). An optical microscope image of the tree geometry is also shown in Fig 9(b). The modes of the tree shaped trival mechanical cavity are optically readout at the horizontal and slanted edges of the tree geometry as indicated by yellow dots.